Title

High-Energy Beta Decay of Light Elements

Permalink

Author

Vedder, James F

Publication Date

1958-06-01

UCRL 8324

cy 2

UNIVERSITY OF CALIFORNIA

Radiation Laboratory

HIGH-ENERGY BETA DECAY OF LIGHT ELEMENTS

UCRL-8324
Physics and Mathematics

UNIVERSITY OF CALIFORNIA

Radiation Laboratory
Berkeley, California

Contract No. W-7405-eng-48

HIGH-ENERGY BETA DECAY OF LIGHT ELEMENTS

James F. Vedder

(Thesis)

June 16, 1958

Printed for the U. S. Atomic Energy Commission

HIGH-ENERGY BETA DECAY OF LIGHT ELEMENTS

Contents

VI. Errors

IX. Appendices

HIGH-ENERGY BETA DECAY OF LIGHT ELEMENTS

James F. Vedder

Radiation Laboratory
University of Califoria
Berkeley, California

June 16, 1958

ABSTRACT

The beta decay of the radioactive members of the mass-eight and -twelve triads has been studied with a spiral-orbit spectrometer having a 1.3% resolution. The end point, half-life and log-ft values respectively are: for N^{12}, 16.37 ± 0.06 Mev, 11.43 ± 0.05 milliseconds, and 4.17; for B^{12}, 13.40 ± 0.05 Mev, 20.6 ± 0.2 msec and 4.11; for B^8, 14 Mev (broad), 0.75 ± 0.02 sec, and 5.72; and for Li^8, 13 Mev (broad), 0.87 ± 0.01 sec, and 5.67. The mass excesses in millimass units are: for N^{12}, 22.48 ± 0.06; for B^{12}, 18.19 ± 0.06; for B^8, 27.08 ± 0.13; and for Li^8, 24.97 ± 0.09.

The shapes of the Kurie function for the mirror pairs indicate positron and electron transitions to the same levels of the daughter nuclide, with greater percentages in the positron branches relative to the ground-state transitions because of the higher energy available. The Li^8 and B^8 shapes are consistent with the shape of the alpha spectrum following the decay of the Be^8 daughter. Less than 1% of the Li^8 transition and less than 5% of the B^8 transition go to the Be^8 ground state. Besides the main transition to the broad 2.9-Mev level, a broad level near 11 Mev is probably involved. The ft values and the assumption of J=0, 2, and 4 levels in Be^8 favor J=3 for Li^8 and B^8. The N^{12} and B^{12} spectra indicate transitions of a few percent to the 4.43- and 7.65-Mev levels in C^{12}, with higher levels not excluded. For these nuclides J=1 is favored.

The agreement of the measured end points and resulting Q values with published values shows that the spiral-orbit spectrometer can be accurately calibrated with only the theory as a guide. Another evaluation of the spectrometer is that the measured shape of the B^{12} Kurie function

is the same within statistics as that obtained elsewhere with a ring-focus magnetic-lens spectrometer.

I. INTRODUCTION

The measurement of the high-energy beta-decay spectra from the beta-radioactive members of the Li^8-Be^8-B^8 and B^{12}-C^{12}-N^{12} isobaric triads is interesting for a number of reasons. The maximum electron energies determine the mass differences of the parent and daughter nuclides. These energies along with a measurement of the half lives will then permit the calculation of the ft values, which are a measure of the influence of the nuclear matrix elements of the transitions and lead to classification into the various allowed and forbidden categories.[1] Any branching in the transition will locate excited states in the daughter nucleus, and one can compare the mirror nuclides to determine whether they decay as expected to the same states of the daughter nucleus.

A great deal of work has been done on Li^8 but little on B^8. The Li^8 spectrum, showing a complex Kurie plot, has been measured in a magnetic-lens spectrometer.[2] The shape is consistent with a transition primarily to the broad 2.9-Mev level in Be^8 and shows about 10% branching to levels above 9 Mev. For B^8, Alvarez determined the half life and maximum energy of the positrons in coincidence with alpha particles from the Be^8 breakup and concluded that the transition is to the same level in Be^8 as the Li^8 transition.[3] Gilbert found the alpha spectra from the decay of Be^8 following the Li^8 and B^8 beta decay are similar within his statistics and give evidence of excited states in Be^8 above the 2.9-Mev level.[4]

As for the other set of triads, much work has been done on B^{12} but little on N^{12}. The B^{12} spectrum has been measured[2] and the branching studied quite intensely.[5,6] In part this interest arises from the fact that the B^{12} decay is an advantageous means of reaching the 7.65-Mev level in C^{12}, which is of importance in theories of the cosmic abundances of the elements.[6] Most of the transition is to the ground state of C^{12}, and the rest to several excited levels. In the N^{12} decay,[7] in addition to measuring the lifetime and maximum energy of the positrons, Alvarez has found delayed alpha emission indicating that a complex Kurie plot is expected for this nuclide also.

The spiral-orbit spectrometer[8, 9, 10] with its large-solid-angle focusing was selected for the spectral measurements. The principle of this instrument is based on the fact that a charged particle of a certain momentum originating at the axis and traveling in the plane of symmetry of a nonhomogeneous axially symmetric magnetic field spirals out to a circle of fixed radius ρ. By placing a detector at this radius, whose magnitude depends only on the magnetic-field shape, and varying the field, one can intercept particles of various momenta. It was possible to detect positrons and electrons simultaneously with an arrangement of two sets of Geiger tubes in coincidence on the focal circle. Fortunately, by using targets of beryllium or C^{13}-enriched carbon bombarded in the beam of the 32-Mev Berkeley proton linear accelerator, one can produce Li^8 and B^8 or B^{12} and N^{12}. Thus simultaneous detection of the mirror decays is feasible. Since the half lives of the elements studied are so short, all less than 1 sec, it was necessary to create the activity at the source position of the spectrometer. Therefore the magnet was located so that the proton beam came down the axial hole in the magnet, and the counting was done between proton pulses.

II. APPARATUS

A. General Layout

The experimental work was performed at the Berkeley 32-Mev linear accelerator. The proton beam from the accelerator enters the concrete-walled bombardment area (shown in Fig. 1) and is bent 20 degrees horizontally by a steering magnet. Three feet farther downstream the protons pass through an adjustable aluminum iris set for a 1/8-in.-square collimation. The target, located in the median plane of the spectrometer, is 6.5 ft beyond. In the upstream brass tube of the vacuum chamber is located a 1/8-in. i.d. carbon collimator (Fig. 2) whose exit is about 3 in. from the median plane.

After passing through the target, the beam travels down the exit brass tube, through the end window, and into the Faraday cup. The charge is measured by an electrometer and a Speedomax recorder.

B. Spiral-Orbit Spectrometer

Dr. Miyamoto developed a magnetic spectrometer[8] with a nonhomogeneous axially symmetric magnetic field in which the charged particles travel in spiral orbits from an axially located source to a focal circle (Fig. 3). Its great advantage over other spectrometers is the large-solid-angle focusing. The conditions are such that particles leaving the axis in all directions in the median plane with momentum $p = mv = eH(\rho)\rho$ approach a circle of focus of radius ρ, where ρ is determined from the equation

$$H(\rho)\rho^2 = \int_0^\rho H(r)\,rdr.$$

Those of greater momentum pass through and are lost, while those of less momentum turn back before reaching the circle. For low-intensity activities it is also possible to take advantage of z focusing because ρ is in the fringe field region outside the radius of the pole pieces. The solution of the equations of motion will lead one to these conclusions as well as to the shape of the resolution function of the spectrometer.[9,10] The theory is outlined in Appendix A. Note that the position of ρ is independent of the magnitude of the magnetic field. Thus it is possible to detect particles within a small momentum interval that are emitted near the axis at all angles in the median plane simply by placing a

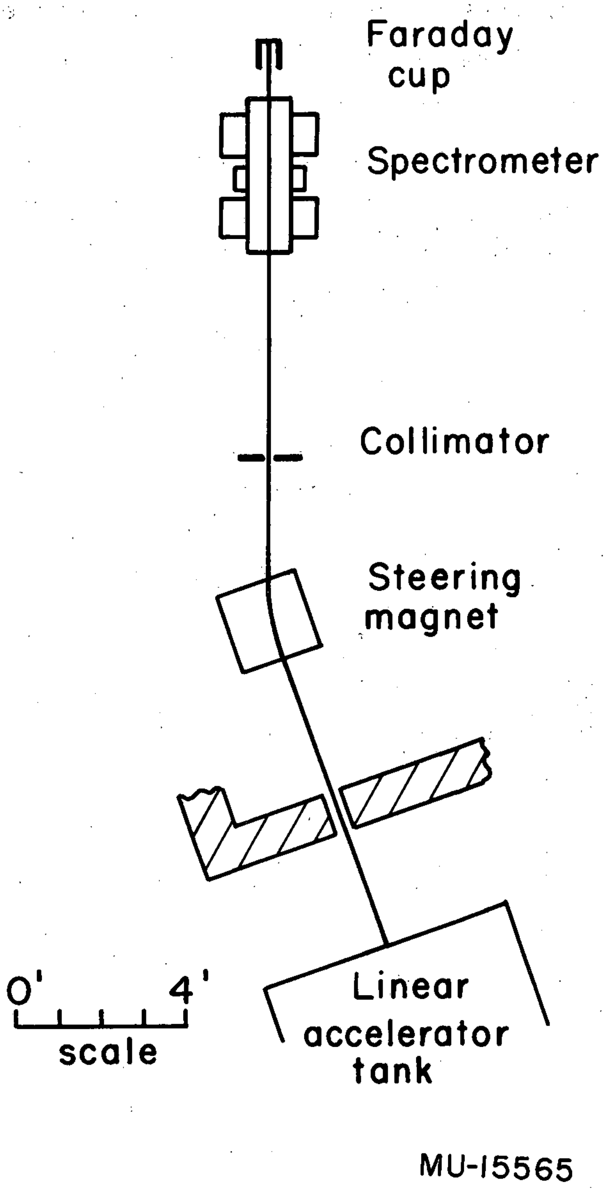

Fig. 1. View of bombardment area.

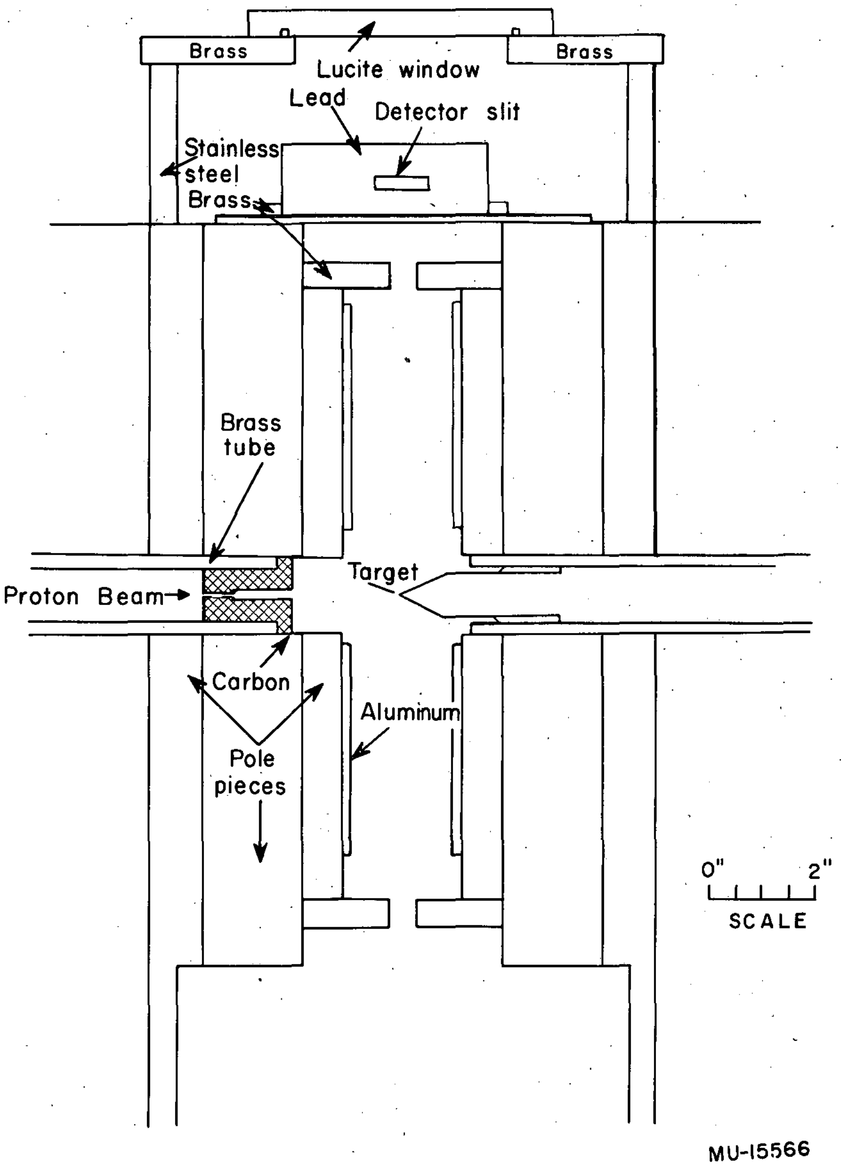

Fig. 2. Cross section through spectrometer. The pole tips, target, slits, detector, and vacuum chamber are shown.

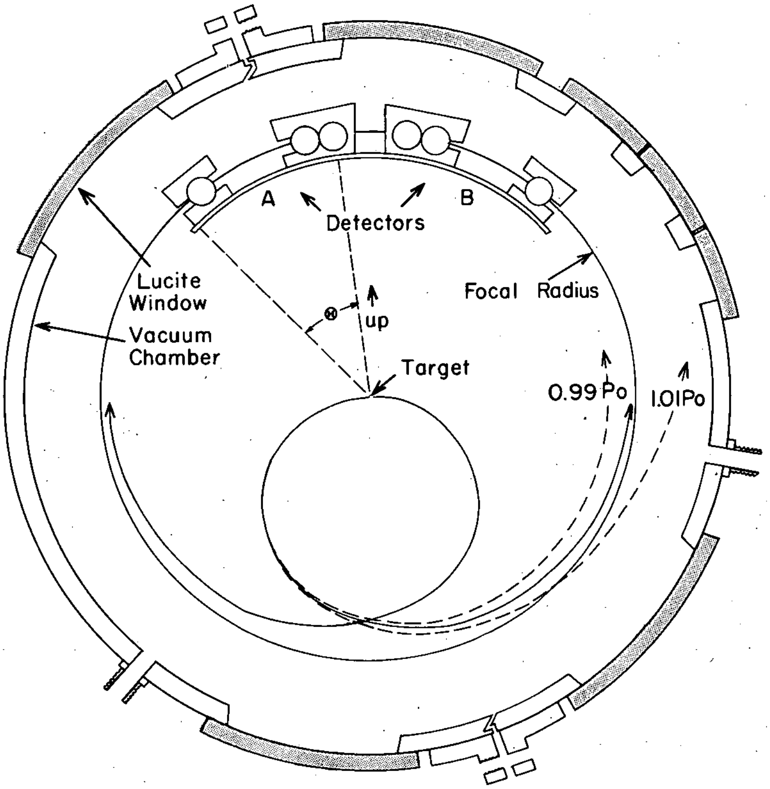

MU-15567

Fig. 3. Median plane of spectrometer. The vacuum chamber, detectors, and several orbits are shown.

suitable detector in the focal circle. Different momenta are measured by the usual procedure of varying the magnetic field. The radial field distribution is not too critical but is usually shaped to obtain focusing properties suitable to the particular experiment. For large-z focusing, a field decreasing with r over most of the orbit is desirable, whereas for high resolution, a fairly flat central portion and then a steep fall-off with r is better. One must be careful that saturation effects do not change the shape of the magnetic-field distribution as the field is changed, since these can seriously alter the detection probability and energy calibration.

The particular electromagnet used for the spectrometer has a 14-in. o.d. iron core with a 1.5-in. axial hole through it. A 5-kw motor generator set, coupled with a current regulator capable of better than 0.1% regulation, energized the pole windings. Facing the gap are several special pole pieces (Fig. 2). Following the core and windings is a pole piece designed to serve as part of the vacuum chamber. It consists of a 14-in. o.d. by 1-in.-thick soft-iron disk to which a 0.5-in.-thick nonmagnetic stainless steel ring, 20 in. o.d. and 14-in. i.d., is welded flush with the face toward the core. The use of stainless steel rather than soft iron is a precaution against nonuniform saturation effects, which could change the field shape and, consequently, the position of the focal radius. Next comes a pole piece, 14 in. o.d. by 1.875 in. thick. Three bolts extending down through the yoke and the core screw into blind holes in this disk. Finally, facing the gap and attached to the preceding piece, is a pole tip, 11.5 in. o.d. by 0.75 in. thick, which creates a slower fall-off of the magnetic field intensity with increasing radius. This piece is covered with 1/8-in. aluminum to reduce scattering. Across the 2-in.-wide gap is a similar pole geometry.

The radial magnetic-field distribution in the median plane is shown in Fig. 4. The dip in the center is caused by the axial hole. Also shown are the vector potential and the product of field and radius. The intersection of the last two curves illustrates the graphical method of determining the focal circle. Several typical orbits for particles originating from the axis are shown in Fig. 3.

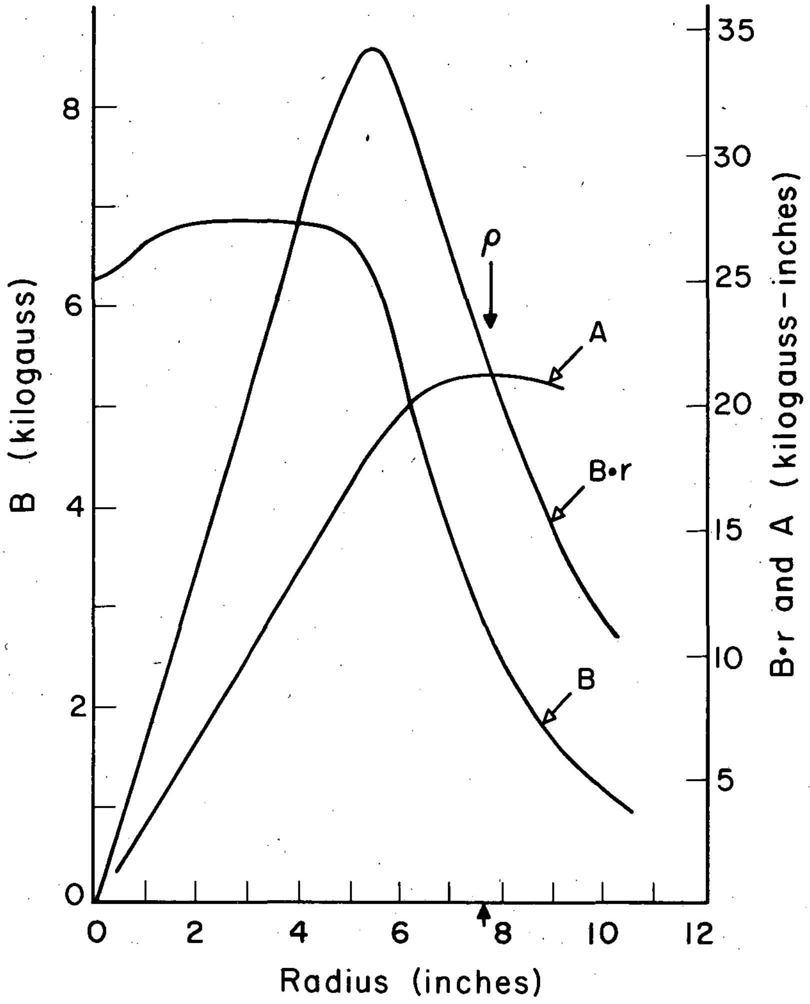

MU-15568

Fig. 4. Radial distribution of the magnetic field, vector potential, and B· r corresponding to 15.6 Mev. The intersection of A and B· r determines ρ.

The vacuum chamber consists of several parts (Figs. 2 and 3). The special pole tips mentioned above have an O ring (on the gap side) located at a radius outside the bolts holding the pole tips. On the outside circumference is another groove for a Hycar gasket. Around this and enclosing the gap is a 0.5-in.-thick brass cylinder separable into two halves which, when bolted together, pull down on the 20-in.-o.d. pieces and the appropriate gaskets to form a tight seal. In this brass cylinder are several openings covered with Lucite windows, permitting access inside the chamber and pass-through connections for the various Geiger-tube cables. A 1-in.-i.d. brass tube with O-ring seals is fitted in the axial hole of each magnet pole. One provides a beam entrance and vacuum connection to the linear accelerator, and the other an exit to the Faraday cup for the protons after passing through the target. There is a cap with a 0.001-in.-thick copper foil window over the exit end of the tube. A mechanical vacuum pump attached to a pump-out connection on the brass chamber was used to pump the system down before the port to the linear accelerator was opened.

The most suitable shape for the targets in this particular experiment was conical, with the axis coinciding with the magnetic axis and the collimated proton beam. This form permitted a compromise between minimizing the energy loss of the electrons in the target and exposing a maximum number of target nuclei to the proton beam, and allowed the use of a target holder that would not be struck by the protons or focused electrons. Not in this experiment but in some cases, such as determining an excitation function, one would also want a minimum loss of energy by the protons in the target. Here again the conical target would be advantageous. The central half-angle of the cone is 25°, determined by a steel mold available from a previous experiment. The cones were attached to thin-walled polyethylene cylinders, 0.875 in. in diameter, extending out about an inch from metal cylinders that slide inside the axial brass tubes of the vacuum chamber. This provided accurate centering and a quick method of changing targets through the rear of the magnet. Because the 0.001-in. beryllium foil available was too brittle to form a cone, a four-sided pyramid with a wall thickness of 0.002 in. was constructed and attached as above. The C^{13}-enriched carbon was packed in the tip between two 0.002-in.-thick polyethylene cones separated by a truncated cone (0.004 in. thick in one case, and 0.015 in. in the other) (Fig. 5).

For better momentum selection one must use defining slits. To limit the aperture normal to the pole faces and thus discriminate against electrons having a z component of momentum, there is a 0.5-in.-wide annular slit defined by 0.5-in.-thick brass rings around the 11.5-in. pole tips. (Fig. 2). Since the magnetic field distribution (Fig. 4) is fairly flat inside this radius, one expects little z focusing in this region.

At the detector (Figs. 2 and 3), consisting of three Geiger tubes in coincidence, is another slit system. The tubes are housed in lead shielding with 1.25-in. slits of 0.25-in. radial width. The central angle from the first slit and tube to the second slit and tube is about 25 degrees. The last two tubes are mounted as close as possible in one lead housing. This arrangement was designed to minimize scattering and yet give good discrimination against background originating outside the target. Because it was desirable to count both positrons and electrons at the same time to conserve running time, there is a similar detector system back to back with this one.

The counter slits are centered on a radius of 7.75 in., a value based on preliminary magnetic-field measurements. The actual focal radius is at 7.71 in., with the result that a small energy correction is required; this is discussed later. The lead counter housings are mounted on a 1/8-in. brass plate curved to rest on top of the 14-in. pole pieces. In view of the possible necessity of frequent changes in the counting tubes, the counter housings had to be made easily removable through the 4-by-5-in. windows of the vacuum chamber. By means of guides and stops, replacement of parts was made reproducible to better than 0.01 in.

In order to detect the beta particles, Victoreen 1B85 Geiger tubes were used. These 0.75-in.-diam. cylindrical aluminum tubes have a wall thickness of 30 mg/cm^2. Only the central 1.25 in. of the 2-in. sensitive length is used. A good tube when new has a plateau from about 800 to 1,000 volts with a slope of 3% per 100 v for

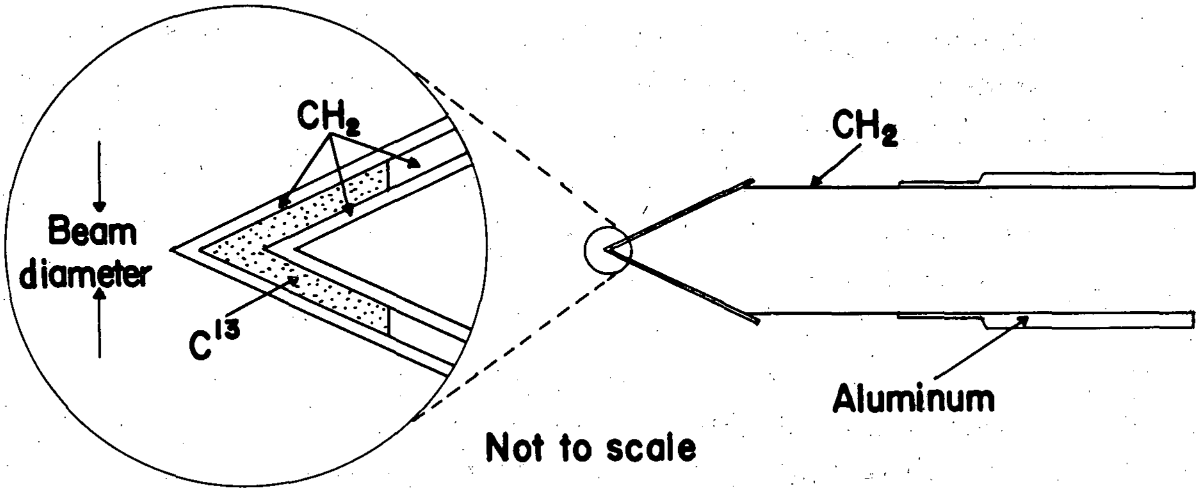

MU-15569

Fig. 5. Cross section of target holder and C^{13} target.

about 150 v of this range. As the useful counting lifetime of the tube is used up, the plateau becomes less flat and shifts towards higher voltages. Before use, a tube's plateau was determined, and usually before a day's run each tube was rechecked. Occasionally tubes would not last the normal lifetime. This may have been a result of the use inside a vacuum. It is conceivable that minute leaks may appear when the external pressure is less than the internal pressure of the tube.

Because the tubes were operated in a magnetic field during the experiment, tube response under these conditions was carefully studied. The observation of the oscilloscope traces of the pulse shape and height revealed no significant differences when the magnetic field was changed from zero to a value above those reached in the spectral measurements. As another check, the plateaus of two tubes were measured at zero and at a high field, and again no significant difference was noted.

Actually the conditions are better than they seem. The particles detected in coincidence are restricted by slits and pass near the central wire of the Geiger tubes. For such conditions, the plateaus should be flatter and a bit longer. With only the central portion of the tube irradiated, a fairly good plateau resulted for a tube previously rejected when the plateau was measured with over-all exposure to radiation.

The dead time is a limiting factor in the singles counting rates, and care must be taken not to jam the counters with high particle fluxes. The dead time can be observed on an oscilloscope or measured by use of two sources.[11] The values obtained are about 200 microseconds. Another check on counter overloading and a method of measurement of the dead time of the coincidence system results from the half-life measurements of the activities. If the data points early in the life fall below the straight line on the semilogarithmic plot (Fig. 6), saturation of the counters is taking place. From the singles counting rate and the difference between the data and straight line, one may calculate a dead time of about 150 to 200 μsec. During the experiment the singles counting rate was monitored as a precaution against overloading the detectors.

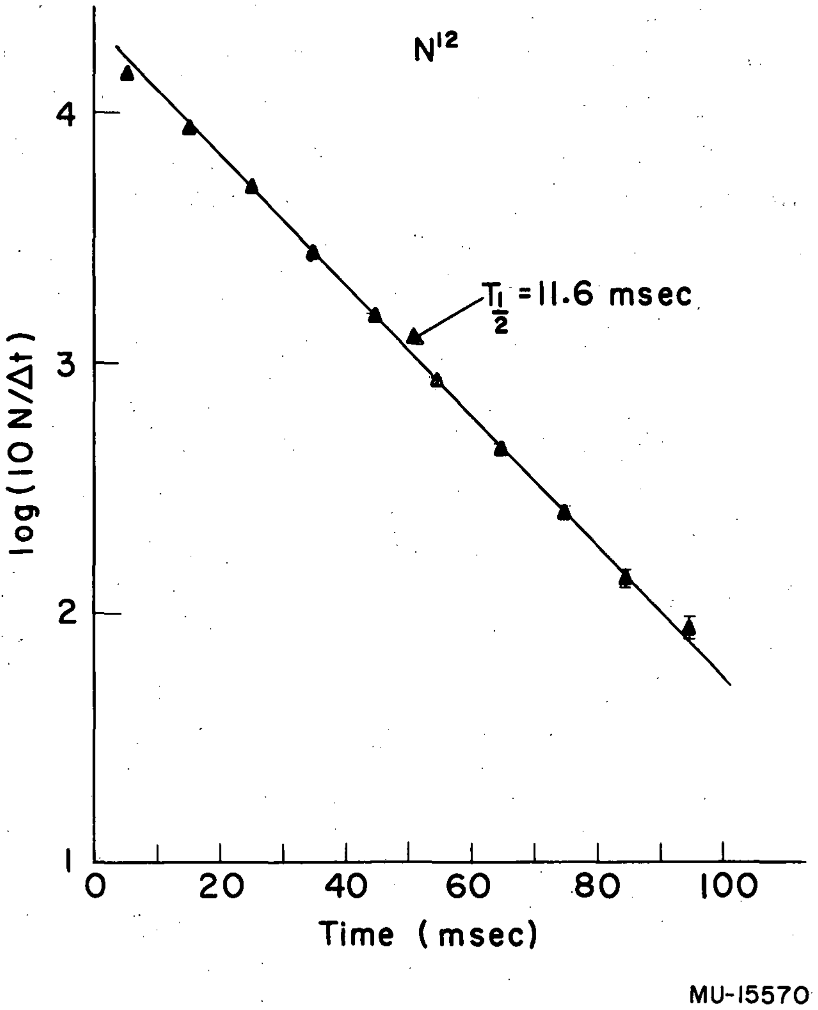

Fig. 6. Example of a decay curve for N^{12} (Run 3).

C. Electronics

The electronic circuitry was quite simple (Fig. 7). The negative Geiger-counter pulses were attenuated and fed into a linear amplifier. The positive output pulses were shaped into 2-μsec square pulses by a variable-gate and variable-delay unit and then fed into a mixer to obtain triple coincidences. The coincidence output was paralleled into the desired number of scalers. A scaler-gate unit provided gates which activated the scalers and a five-channel tandem-gate unit. The tandem-gate unit produced five gates in succession. The scaler-gate unit produced a gate that triggered the tandem gate. For N^{12}, with the linear accelerator running at the normal repetition rate of 15 pulses per second (66.7 msec between pulses), the scaler-gate unit was triggered by the linear-accelerator trigger and was set to give a 50-msec gate delayed about 10 msec. This gated one scaler to give a total count and triggered the tandem gate which was adjusted to give 10-msec gates. Thus the scalers counted over about five lifetimes, with one scaler recording the sum as a cross check. To get a good half life, a second tandem-gate unit was triggered at the end of the first five gates, and with a linac repetition rate of 7.5/sec about ten half lives could be covered. For B^{12}, the same arrangement as for N^{12} was used during the spectral measurement. In order to get the half-life data, a 3.75/sec rate and ten tandem gates were used to cover about ten lifetimes.

For B^8 and Li^8 with lifetimes of about 0.8 sec, some modifications had to be made in the triggering and gating. A scaler counted the 15-per-sec machine trigger pulses, and the scale-of-16 output fed a modified scaler. By means of relays the latter controlled a cycle as follows: 16 pulses (1.067 sec) of accelerated protons, 112 pulses (7.467 sec) in which the Van de Graaff phasing was shifted so that no protons would be accelerated by the linear accelerator, restoration of the proper phase, and repetition of the cycle. The various gates were triggered by the modified scaler to operate during the beam-off time.

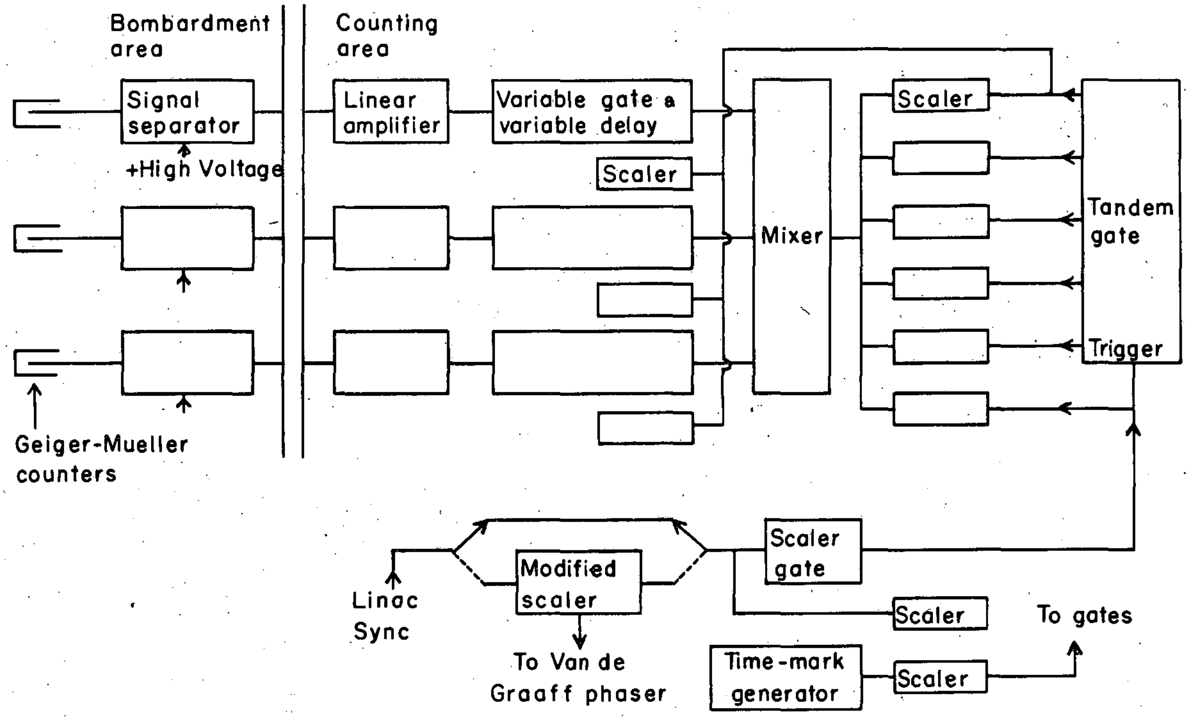

MU-15588

Fig. 7. Block diagram of electronic circuitry.

III. OPERATIONAL PROCEDURE

A. Spectra

In making the spectrometer current settings, great care was taken to follow as nearly as possible the same magnetization curve. Spectral data was taken only at field values reached by increasing the forward or reverse current. A Leeds and Northrup potentiometer permitted adjustment of the current to about 0.1%, and the current regulator held it to this accuracy once the magnet and windings were warmed up.

In the measurement of a spectrum, the current settings were made so that counting data were taken at every other or every fourth electron energy of the chosen series during a particular quarter cycle of the magnetization curve. The other points were covered in following cycles on both the increasing forward and reverse currents. We believe this procedure minimized the effects of possible drifts and fluctuations on the experimental data. It also alternated the measurement of a particular spectrum from one detector system to the other with each current reversal. In case a normalization was needed for combining the data from the various cycles, a selected point near the maximum counting rate was repeated each quarter cycle. Data were taken at each point for a sufficient number of microcoulombs of proton beam collected in the Faraday cup to give 5 to 10% counting statistics at the peak counting rate. In all, each measurement, excluding the normalization point, was repeated three to six times for a complete spectrum measurement.

B. Lifetimes

For the half-life determinations, the current was normally set for an energy giving a maximum counting rate. Some data were also taken at higher and lower current settings to check for contaminations by other activities. Counts were taken in consecutive gates extending out to about 10 half lives for each nuclide. The linear accelerator was run at the proper pulse rate or cycling, and the widths of the gates were set to better than 1% with the aid of an oscilloscope calibrated with a Tektronix type-180 time-mark generator. For greater accuracy, one gate at a time gated a scaler that counted the output from a time-mark generator which permitted at least 1000 pips per gate width. Another scaler recorded the number of gates during a given run. The number of marks divided by the product of frequency and number of gates gives a good width calibration, and indicates any drifts in widths during the data-collection time.

IV. DATA REDUCTION

A. Theory of Beta Decay

In order to obtain the theoretical shape[12] of a beta-decay momentum spectrum, one starts from a general formula for the transition rate from an initial state into a continuum of states:

$$R = \frac{2\pi}{\hbar} \overline{|H|}^2 \frac{dn}{dW_0} .$$

Here H is the matrix element of the perturbation causing the transition. The statistical factor, dn/dW_0, is the number of final states per unit interval of the energy release $W_0 = W + W_\nu$, where W and W_ν are the total energies of the electron and neutrino. Thus we have

$$\frac{dn}{dW_0} = \frac{p^2\, dp\, d\omega}{(2\pi\hbar)^3} \cdot \frac{q^2\, d\omega}{(2\pi\hbar)^3 c} ,$$

where p and q (equal to W_ν/c) are the momenta of the neutrino and electron respectively. Integrating over the solid angles and substituting into R, we obtain:

$$R = N[p]dp = C\, \overline{|H|}^2\, p^2\, (W_0 - W)^2\, dp$$

or

$$N(p) = C\, |M|^2\, F(Z, p)\, p^2 (W_0 - W)^2 ,$$

where M is the matrix of the nuclear transition, and $F(Z, p) = |\psi e(R)|^2$ is the Coulomb factor that distorts the statistical shape by the interaction of the Coulomb field of the electron and daughter nucleus. For data analysis it is more convenient to work with the Kurie form of the equations,

$$W_0 - W = \sqrt{\frac{N(p)}{F(Z, p) p^2}} .$$

Plotted against W, this is a straight line for a purely statistical shape, and its intersection with the energy axis gives the upper limit of the spectrum.

The Coulomb factor is small for low-Z nuclides and high-momentum electrons. For these conditions a simplified equation can be used.[13] Figure 8 shows that the Coulomb factor changes the shape of the Kurie function by only a few tenths of a percent at most over the energy range of interest.

A quantity that aids in determining the forbiddenness of a transition is the log ft value. Here f is the energy integral of the statistical factor modified by the Coulomb factor, and t is the half life. The ft value is inversely proportional to the nuclear matrix elements and thus is a measure of their influence on the decay probability. The "favored" transitions have log ft = 2.7 to 3.7.[1] The normal allowed transitions fall on the range 4 to 5.8. Moszkowski[14] presents a rapid method for calculating log ft values. He separates the quantity into a main term log f_0t plus correction terms for the Coulomb factor and for branching. The f_0 is simply the energy integral over the statistical shape and is a measure of the decay probability if the Coulomb factor and nuclear effects are neglected. The partial half life for transitions is accounted for by the branching correction.

The maximum energy W_0 is determined by the mass difference between the parent and daughter nuclides. For electron transitions, the atomic-mass difference or Q value is equal to $W_0 - m_0c^2 = T_0$, the maximum kinetic energy. For positron emission $Q = W_0 + m_0c^2 = T_0 + 2m_0c^2$.

In order to obtain a momentum spectrum from the spectrometer data, one must divide the counts by the corresponding momentum or something proportional to it, because the width of the resolution function is proportional to the momentum focused. In this experiment the maximum value of the magnetic field in the median plane is used instead of the actual momentum. A calibration curve of the spectrometer-excitation current against the magnetic field was established and the corresponding focus energy calculated. The absolute accuracy discussed in Section VI is about 0.3%. For each current setting, the Kurie function with the momentum replaced by the corresponding magnetic field is calculated and plotted against the kinetic energy; field and energy were obtained from the calibration curve. Because the detector positions were not centered on the focal orbit and because of a slight magnetic-field asymmetry, there are two corrections to the energy calibration. These are evaluated in Section VIA.

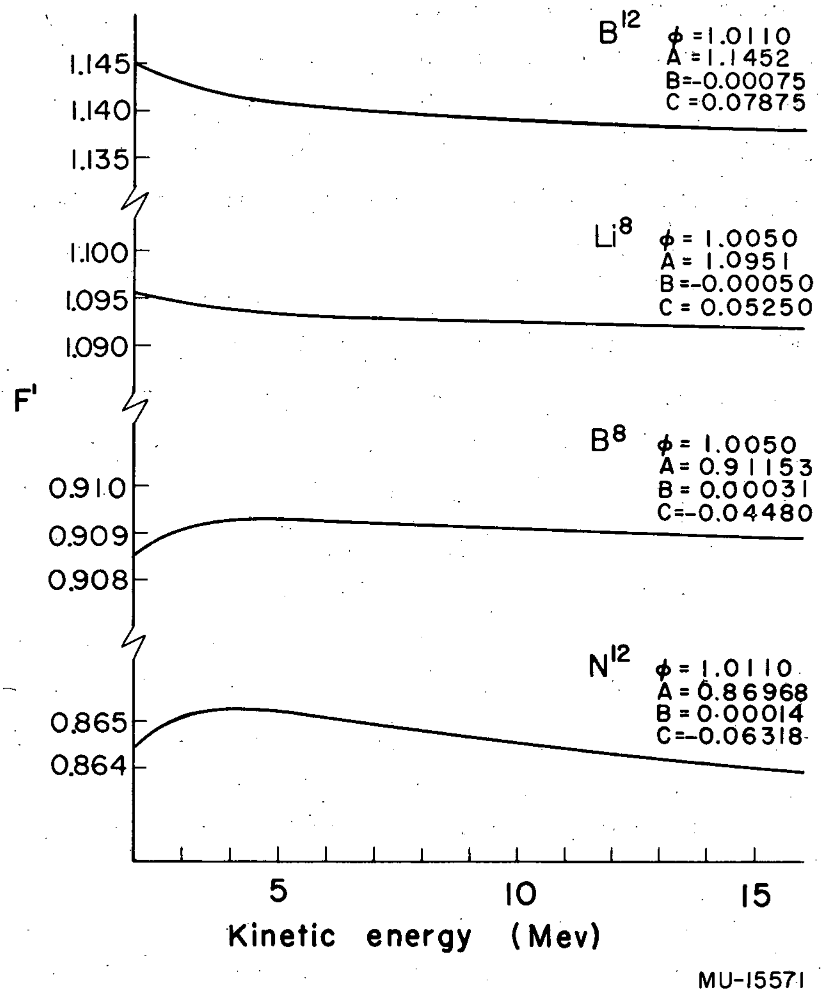

Fig. 8. Coulomb factor in beta decay.
$F' = F(Z, \eta)/\phi(Z) = \eta^{2S}(A + B/\eta + C/\eta^2)$ $\eta = p/m_\theta C$,
$S = [1 - (\alpha Z)^2]^{\frac{1}{2}} - 1$. Good to about 1% above 3 Mev.

B. Statistics, Errors, Least-Squares Fit

In the treatment of data, the work of Birge is followed.[15] He discusses statistical errors, propagation of errors in functions of measured quantities, and fitting of data. If the true errors X of a sample of n observations are known, the root-mean-square error or standard deviation is $n^{-\frac{1}{2}}(\Sigma X^2)^{\frac{1}{2}}$. If the error distribution is Gaussian, there is about 30% probability of exceeding the standard deviation. In most cases the true errors are not known, but the method of maximum likelihood gives us an estimate of the error from the residuals V, the difference of the measured values from the mean. Thus an estimate of the standard deviation is $(n-1)^{-\frac{1}{2}}[\Sigma V^2]^{\frac{1}{2}}$. There is a distinction made between internal consistency and external consistency of data. Errors based on internal consistency are derived from the propagation-of-errors formula and are a measure of the agreement to be expected among several measured quantities. On the other hand, errors based on external consistency are obtained from the consistency of the data and are a measure of the actual agreement of the data. For the weighted mean of n points--weights being assigned inversely proportional to the square of the error--the consistency is evaluated from the residuals, and the expression for the root-mean-square error is

$$\left[\frac{\Sigma p_i V_i^2}{(n-1)\Sigma p_i}\right]^{\frac{1}{2}},$$

where p_i is a weight. By internal consistency, the error is found to be $[\Sigma p_i]^{-\frac{1}{2}}$. If the errors are purely statistical, the ratio of the former to the latter should be unity, aside from statistical fluctuations expected in the ratio. If there are systematic and nonstatistical errors, the ratio will be greater than one. In this experiment estimates of the standard deviation based on external consistency are used unless the error by internal consistency is much larger. For most cases the ratio is close to unity. The error for the maximum energies, or Q values, is based on internal consistency, because only a few numbers are averaged, and the error is equal or less by external consistency.

In the determination of the maximum energies, lifetimes, and backgrounds, a weighted least-squares straight line is fitted to the data.[15]

In most cases the straight line involves the logarithm or square root of the observed data, and care must be taken to obtain the proper weight. Application of the formula for propagation of errors gives the error of the function in terms of the errors of the observations. The weight is then inversely proportional to the square of this error. The expressions used to obtain a least-squares fit of a straight line to the experimental data were

$$y = a_0 + a_1 x,$$

$$D \cdot a_0 = \Sigma p_i x_i^2 \cdot \Sigma p_i y_i - \Sigma p_i x_i \cdot \Sigma p_i x_i y_i,$$

$$D \cdot a_1 = \Sigma p_i \cdot \Sigma p_i x_i y_i - \Sigma p_i x_i \cdot \Sigma p_i y_i,$$

$$D = \Sigma p_i \cdot \Sigma p_i x_i^2 - (\Sigma p_i x_i)^2,$$

where x_i and y_i are the measured values of the abscissa and ordinate of the ith point and the x_i values are assumed to have no error. In addition the following relations were used to analyze the experimental data:

Kurie end point:

$$T_0 = -a_0/a_1,$$

$$\text{Error} = (r_0/a_1) \left[\frac{\Sigma p_i x_i^2 - 2\Sigma p_i x_i \cdot T_0 + \Sigma p_i T_0^2}{D} \right]^{\frac{1}{2}} .$$

Half Life:

$$T_{\frac{1}{2}} = -0.69315/a_1 ,$$

$$\text{Error} = 0.69315(r_0/a_1^2) \left[\frac{\Sigma p_i}{D} \right]^{\frac{1}{2}}$$

Error of single observation of unit weight by external consistency:

$$r_0 = \left\{ \Sigma \frac{p_i[y_i - y(x_i)]^2}{n-2} \right\}^{\frac{1}{2}} .$$

C. Lifetime

Several calculations are required for the half-life reductions. First the mean gate widths and their uncertainties are determined from the calibration data. Then the accumulated counts in each gate are divided by the gate width to obtain a counting rate. The time abscissa is calculated from the relation

$$t'_i = t_i + \tau/n \ \{a/[1-\exp(-a)]\}.$$

This expression is derived for an assumed mean life τ by equating the counting rate calculated for a gate width $\Delta t = a\tau$ to the instantaneous counting rate at time t' and solving for t'; t_i is the time origin of the ith gate, obtained by summing the preceding gate widths.

An error in the assumed value of τ shifts each t'_i by a constant amount if the Δt are equal. Even if the Δt are only approximately the same, the error introduced in the time scale is small. For example, in a series of gates of 10-msec widths, in which the maximum deviation between gate widths is 0.1 msec, the error in the time scale after a shift for alignment is less than 0.01 msec when $\tau = 29$ is used instead of $\tau = 16.6$ msec. For B^8 and Li^8 each gate maintained its width to less than 1% deviation from the mean, and those for N^{12} and B^{12} held to less than 0.5%. Assuming the maximum deviations, one finds that the time abscissa of the first gate is uncertain by about this percentage, and the last of ten gates is uncertain by about one-third of this percentage.

After corrections for background, if any, have been made, a weighted least-squares line is fitted to the data for $\ln(N/\Delta t)$ versus time, with the assumption that the time scale is exact. The uncertainty of the gate width is included with the counting statistics in determining the proper weights. The error in the time scale has been combined with the error in the mean value of the lifetime. Only for N^{12} is this addition of any significance.

D. Spectra

1. Accidentals and Dead Time

In the reduction of the spectral data there are several effects that must be considered. Accidental coincidences, counter dead-time losses, drifts, background, and electron scattering are included in the recorded counts. The spectrometer resolution and the ionization and radiation by the electrons in the target are involved in the energy measurements.

The correction for accidental counts is negligible. In the determination of accidentals, delays were introduced before the mixer; and the coincidence counting rate was determined. The result was essentially zero.

The dead time of about 200 microseconds characteristic of the Geiger tubes causes a significant loss of counts if the counting rate is too high. During the experiment the singles rate was kept low by using enough delay following the proton pulse and--if necessary--using a reduced proton current. The singles counts were monitored and maintained below a 1% loss level during the first tandem gate, whose width was one-fifth or less of the total counting interval. Because the highest singles rates occur closest to the beam, the correction for the total counts is even smaller than for the counts from the first gate. Therefore no corrections have been made for the dead-time losses. The lifetime measurements are another check on the dead-time losses because they indicate the singles rate that can be tolerated without distorting the straight-line semilog plot of counts against time.

2. Drifts and Combination of Data

As mentioned before, a certain spectral point was repeated in each run to provide a normalization point in case of any drifts. Various sources of drift are discussed in Section VI. The ratio of the external to the internal consistency of the weighted mean of the counts at this energy was close to unity for any particular target and activity. This indicated that the effects of drifts, if any, were small, and the data could be added without normalization. Therefore for each target and detector channel the counts from the successive cycles were totaled at each energy and divided by the corresponding charge collected in the Faraday cup.

3. Background

In all cases a background count extended above the end point of the activities. It was about the same for the various targets and decreased as the focus energy was increased. There are a number of possible sources. The cosmic-ray contribution is practically zero because of the counter geometry and magnetic field. The probability of detecting electrons scattered from the various spectrometer parts should be small for similar reasons. If this were the predominant source, the background data should show the lifetime of the activity being measured. In the N^{12} and B^{12} data there is a time dependence, but the decay rate is too slow. The annihilation radiation from positron activities should be quite small because of the low energies and small probability of making a coincidence. Probably the activities produced by the high neutron fluxes in the bombardment room are the main sources of the background. The fact that the background is about the same for the various targets tends to substantiate this view.

To correct the spectral data, a least-squares straight line was fitted to the points above the maximum energy and extended to lower energies. The counts at each energy were then corrected for this extrapolated background.

A limitation of this method is the accuracy of the extrapolation of the background to lower energies. The data are not sufficient to determine the dependence on the magnetic field other than a tendency to increase with decreasing magnetic field. One might expect this behavior for general background, because at lower fields less is swept out of the detector system. One cannot use the lifetime data to determine the background for the spectral runs because the background level is different under the various operating conditions of the linear accelerator. Fortunately the background is not excessive, and the method used should give a reasonable reduction of the data. Near the peak of the various spectra, the background is about 1% except for B^8, where it is about 3.6%.

4. Scattering Correction

Because a triple coincidence was necessary to reduce the background to a reasonable value, one must correct for the scattering of the electrons by the Geiger counters. Fortunately the measured correction to the counting rate at energies greater than 12 Mev is less than 2% (Fig. 9). The correction becomes quite large at low energies and reduces the accuracy of the spectral data. Within the statistics of the measurement, the positron and electron scattering are the same.

From theoretical calculations[16] for low atomic numbers and energies above 1 Mev, the differential cross section for electron scattering is

$$\sigma = \sigma_R \{1 - \beta^2 \sin^2(\theta/2) + \pi Z \beta \alpha \sin(\theta/2)[1 - \sin(\theta/2)]\},$$

where

$$\sigma_R = (Ze^2/2pv)^2 \csc^4(\theta/2)$$

is the Rutherford cross section. For positrons, Z is replaced by -Z to a first approximation. Therefore for small angles the scattering of electrons and positrons is about the same. Actual calculations of the scattering to be expected from the first tube would be difficult. Because the magnetic field is not homogeneous, particles scattered in various directions are deflected differently. The walls of the tubes are curved and present varying thicknesses to the incident electrons. Another complicating fact is that the trajectories enter the detector at various angles, and an analysis of orbit distributions and probabilities would be required.

Several experimental arrangements were used to measure the scattering, and each involved introducing more scattering material into the detector system. From the standpoint of reproducibility and of least disturbance of the counting geometry, the most suitable method consisted of adding 0.005- and 0.010-in. thicknesses of aluminum before and after the first tube. The counting rates were determined at five electron energies with and without the scatterers. The lead housing necessitated a 3/8-in. separation of the aluminum from the tube. This separation may exaggerate the scattering effect, but tends

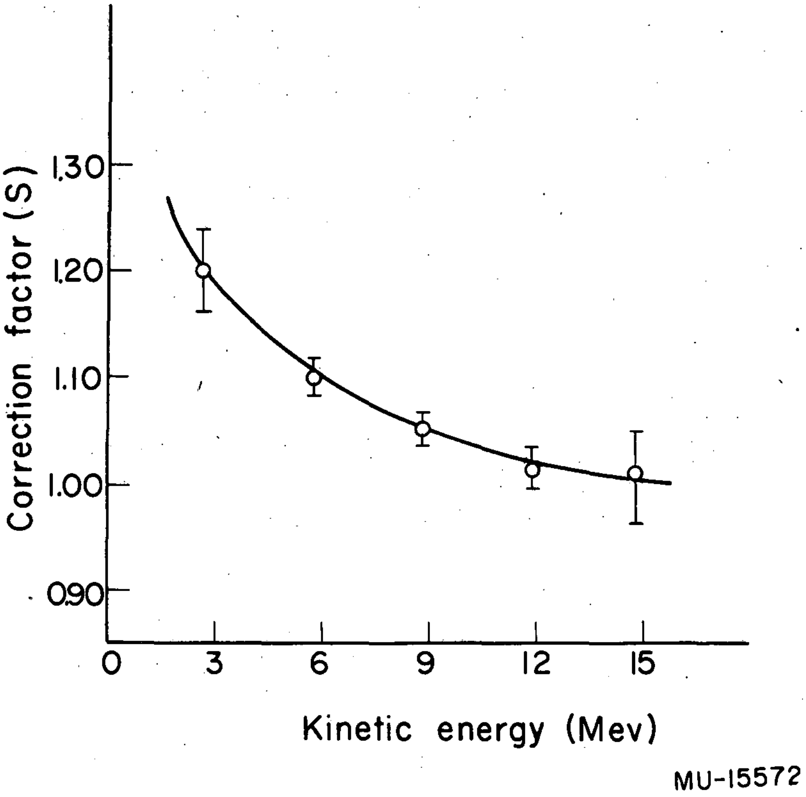

Fig. 9. Scattering correction for Channel A. The recorded counts are multiplied by the appropriate S.

to bring it in line with the effect of the increased mean thickness of the tube wall due to its curvature, a factor neglected in the treatment of the data. Because the last two Geiger tubes were 1/8 in. apart and the counting aperture of the first of the two was restricted by a slit, the scattering loss here should be negligible compared with that from the first tube.

The counting data, consisting of several cycled repetitions at each energy, are plotted against thickness with the assumption that the tube is 0.010 in. thick. A straight-line fit by eye is extended to a zero thickness, and the ratio S of this extrapolated counting rate to the normal counting rate with just the counters in the detector system is then obtained. The accuracy is determined from the consistency of the measurements. To correct the spectral data at the various energies, one simply multiplies by the proper ratio S. A second-degree polynomial was fitted by weighted least squares to the points for Channel A, excluding the lowest-energy point near 3 Mev. The curve for Channel B, which has a narrower slit before the second tube, was obtained by adding to S(A) 10% of the correction S(A)-1. This gives a reasonable fit to the data for Channel B except for one low point at 9 Mev.

5. Energy Loss by Ionization

A second correction is necessary for the electron energy loss by ionization and collision processes in the target. To determine it, one must know the electron path-length distribution, and the most probable energy loss and the energy straggling distribution as a function of the path length. Fortunately there has been some good theoretical and experimental work on this problem, and the ionization loss and straggling distribution are probably known to a few percent in the region from 5 to 20 Mev.

The calculations of Sternheimer are used to obtain the most probable energy loss. He develops equations based on experimental values of the mean excitation potentials.[17] The expression applicable to this work was later corrected to

$$\epsilon_p = (At/\beta^2)\,[B+1.06+2\ln(p/\mu c)+\ln(At/\beta^2)-\beta^2-\delta], \qquad 18$$

and the values to the constants were recalculated on the basis of more recent experimental values of the ionization potentials.[19]

The shape of the energy straggling curve has been calculated by Landau[20] and by Williams,[21] using different methods but obtaining practically the same results. The shape is nearly constant for various energies, materials, and thicknesses when plotted against $(\epsilon-\epsilon_p)/(At/\beta^2)$. The experimental work of Goldwasser et al.[22] agrees well with the Landau distribution and with the most probable energy loss as calculated from Sternheimer's work. In the data reduction, the shape measured by Goldwasser et al. is used with the most probable energy loss as calculated from Sternheimer's equation.

Because the energy corrections are small, one does not need to know the target thickness accurately. For the analysis the pyramidal beryllium target was approximated by a cone having a radial wall thickness of 0.0025 in. For the targets of carbon and polyethylene uniform distribution of the C^{13} was assumed. Because the density of the C^{13}-enriched powder in the target was not known, an experiment was designed to measure it. The attenuation of a beam from a $Sr-Y^{90}$ beta source passing through the target was compared with that for polyethylene of the same shape. From this study an equivalent polyethylene wall thickness was obtained for the two targets used. The radial equivalent thickness for the thin target was 0.0088 in. and for the thick target 0.0188 in. The accuracy of the measurements is about 10%. This is quite sufficient because the mean ionization energy loss for the targets used is less than 1% of the maximum energies of the activities studied.

The path-length distributions for the conical targets were determined by summing the distributions calculated for seven sections within the 1/8-in. beam diameter and defined by planes normal to and spaced at equal intervals along the z axis. Each of these sections, approximated by a cylinder, was divided into five rings of equal radial width. Assuming a source located at the mean radius of the ring and emitting particles in all directions in a plane normal to the axis, one obtains the distribution of lengths from

$$L_i = [R_0^2 - r_i^2 \sin^2\theta]^{\frac{1}{2}} - r_i \cos\theta, \; 0 \leq \theta \leq \arcsin(R_I/r_i)$$

and

$$L_i = [R_0^2 - r_i^2 \sin^2\theta]^{\frac{1}{2}} - r_i \cos\theta - 2[R_I^2 - r_i^2 \sin^2\theta]^{\frac{1}{2}}, \; \arcsin(R_I/r_i) \leq \theta \leq 180^\circ,$$

where $2R_I$ is the inside diameter and $2R_0$ the outside diameter of a section, and r_i is the mean radius of the ith ring. The distribution for the ring is obtained by calculating the $\Delta\theta$ for a given $L \pm \Delta L/2$. The resulting curves of $\Delta\theta$, which corresponds to number of particles, versus L are weighted by r_i, a ring-volume factor, and summed to give the distribution for a particular section. Then all sections are combined to give the path-length distribution (Fig. 10a, c).

There are three small corrections to the path length which have been neglected in the calculations. Multiple scattering increases the path length by a factor $[1 + \frac{L}{\lambda}]$ to give a most probable path length.[23] The λ is a scattering length and the correction is at most a few tenths of a percent for the targets used.[24]

The second is the change in the path length due to the curvature of the trajectory in the magnetic field. But the radius of curvature at the origin for a focused particle is about 3.3 in., and therefore the correction is again negligible for the 1/8-diam. source.

The last one is the change of the path length for angles of emission out of the median plane. The maximum angle is limited to a few degrees by the annular slit. Also, because the cone walls intersect the median plane at an angle, some paths are increased and others decreased. This correction is small compared with the approximations used and has been neglected.

The next step consisted of the folding of the ionization-loss distribution into the path-length distribution. This was done graphically by determining at equal intervals along the path distribution the most probable loss and corresponding straggling curve normalized by area and the path-length probability. The summation of ordinates at intervals in the energy scale then gives the resultant energy-loss distribution of electrons originating in the target (Fig. 10b, d).

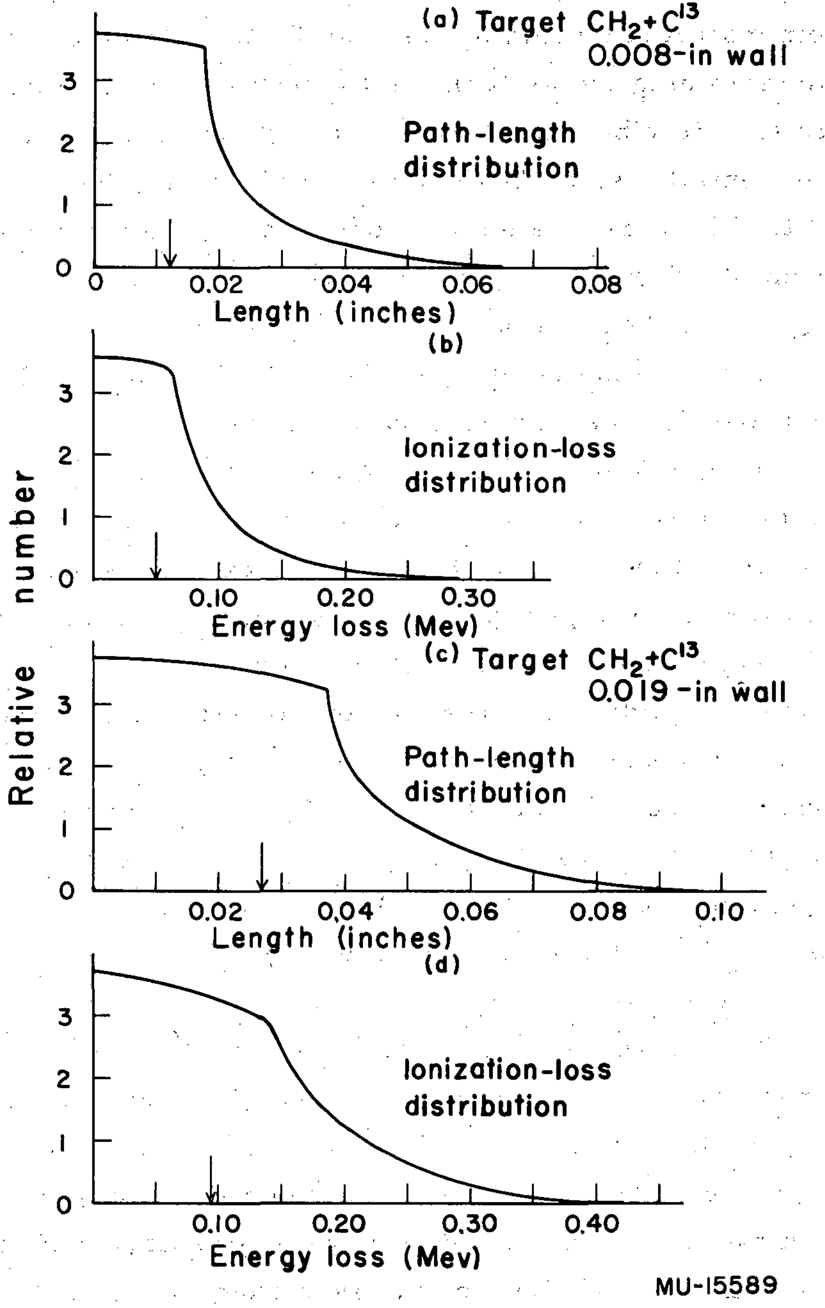

Fig. 10. Path length and ionization-energy loss distributions for the C^{13} targets. The arrows indicate the positions of the ordinates bisecting the areas under the curves.

The effect of the ionization loss on the spectra is to shift the energy scale by an amount approximately equal to the loss, which bisects the area under the energy-loss distribution curve. This may be demonstrated by folding the distribution into a calculated spectrum and determining the shift in the Kurie-function end point. Except where the distribution overlaps the end point, the Kurie function is still essentially straight for an allowed shape. Therefore an energy equal to this half-area energy loss is added to the experimental upper limit obtained from the least-squares fit. The beryllium-target energy correction has been derived from its half-area path length by extrapolation of the relation of the half-area path to the half-area energy loss for the carbon-bearing targets.

To cover many factors, an accuracy of 20% has been assigned to the energy-loss correction of the carbon-bearing targets and 25% for the beryllium target. For the latter, the main errors are the approximation of a pyramid by a cone and the extrapolation of the half-area energy for the path distribution by the use of the thicker-target results as a guide. For the carbon targets, the comparative-thickness measurement and the assumption of uniform distribution of the carbon isotopes are contributing factors. Another assumption that is not exact is that the target energy losses can be treated separately from the spectrometer resolution. But for the resolution used and the losses involved this is a small effect.

6. Radiation Loss

The bremsstrahlung introduces another energy loss that should be considered. Bethe and Heitler have derived expressions for the straggling distributions.[25] For light elements and electron energies in the range of interest, the corrections are negligible and are not used in this reduction. From the experimental standpoint, the work of Goldwasser et al. on the energy-straggling distribution for light elements[22] agrees well with the Landau curve without any broadening needed for radiation losses.

7. Spiral-Orbit-Spectrometer Resolution

There are several data corrections associated with the spectrometer resolution or line shape (Fig. 11). The derivation of this shape for a conical target and a 1/8-in. proton beam is described in Appendix B. For a curve symmetrical about $\Delta B/B = 0$, corresponding to the energy of the focal circle for a given current setting, the theoretical beta spectrum is modified significantly only at the maximum energy within the width of the line shape. For an asymmetric function, one obtains an energy shift of the spectrum equal to the energy difference between the set energy and the energy whose ordinate bisects the area under the curve. Here $\Delta T/T$, $\Delta p/p$, and $\Delta B/B$ are used interchangeably because for the range under consideration the electron energy is proportional to the momentum and therefore the magnetic field. The resolution curve shown is for the slit system centered on the focal circle. The full width at half amplitude is 1.3%. The probability of focusing higher-energy electrons is obtained from the right side of the curve. The asymmetry necessitates an energy correction of 0.043% to be added to T.

There are two other effects that should be mentioned briefly here and are discussed more fully in Section VI. One is the energy shift caused by the detectors' being slightly outside the focal circle, as mentioned before. Since the magnetic field is not quite symmetrical for Channel B the momentum in the focal circle is slightly lower. As a result Channel A requires a 0.3% increase in the calibration energy, and Channel B as a result of the two effects requires a 0.1% reduction in the calibration energy.

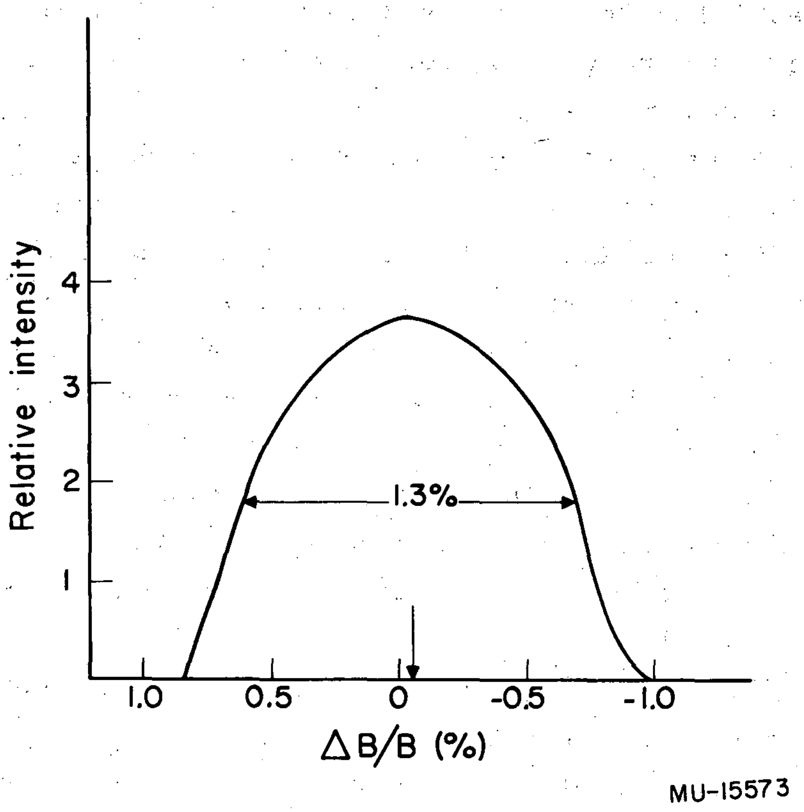

Fig. 11. Resolution function of the spiral-orbit-spectrometer for a 1/8-in. beam and a conical target. The arrow indicates the position of the ordinate bisecting the area under the curve.

V. EXPERIMENTAL RESULTS

A. Boron-8 and Lithium-8

1. Lifetime

Because the lifetimes of Li^8 and B^8 are nearly equal, the same gate widths and linear-accelerator cycling were used for both. The 16-pulse beam-on and 112-pulse beam-off cycle with 15 pulses per second gives about 10 half lives between bombardments. Ten consecutive gates of width 0.7 sec were then triggered to follow the decay of the activities. Several sets of data were taken on different days, and the gates have slightly different calibrated widths.

For the Li^8 decay, the data indicated no need for background subtraction within the statistics of the counts in the final gates. A mean half life of 0.87 ± 0.01 sec is obtained from the least-squares-fit values for the runs presented in Table I. The results of other experiments are also tabulated. The fourth run is shown in Fig. 12. It was necessary to subtract a background to obtain the B^8 lifetime. With a somewhat arbitrary background and a 5-sec half life, fairly consistent lifetime data are obtained from the several runs. Assuming all the counts in the first gate are B^8, one can calculate the numbers to be expected in the final gates. The background is normalized to the difference of the total counts and the calculated B^8 counts in the last few gates. After this component has been subtracted, the least-squares fit is applied. The various runs and the mean half life of 0.75 ± .02 sec are presented in Table II along with results from the literature. The fourth set of data is shown in Fig. 13.

2. Spectra

Because the lifetimes of Li^8 and B^8 are long compared with the normal repetition rate of the linear accelerator, a data-collecting procedure was adopted to conserve running time. In order to determine the purity of the activities, preliminary spectral data were taken in five consecutive gates covering about 2.5 lifetimes during the 2.13-sec beam-off time of a 4.27-sec accelerator cycle. Further evidence was obtained during the lifetime measurements when some data were taken at various energies. This survey indicated that the positron data were consistent with a half life of between 0.6 and 0.9 sec to as low as 2 Mev,

Table I

Li^8 lifetime

This experiment			Other experiments	
Run No.	Half life (sec)	Standard deviation	Half life (sec)	Reference No.
1	0.897	0.012	0.88 ± 0.1	26
2	0.852	0.015	0.88 ± 0.03	27
3	0.896	0.054	0.89 ± 0.02[a]	28
4	0.867	0.019	0.88	29
5	0.824	0.025	0.825 ± 0.02	30
6	0.892	0.028	0.89	31
			0.85 ± 0.016	32
			0.89 ± 0.01	33
			0.875 ± 0.02	34
			0.841 ± 0.004	35

Weighted mean of the half life is 0.873 ± 0.013 sec. which includes 0.75% error in time scale.

---

[a] A footnote in Reference 30 indicates that this value may be high.

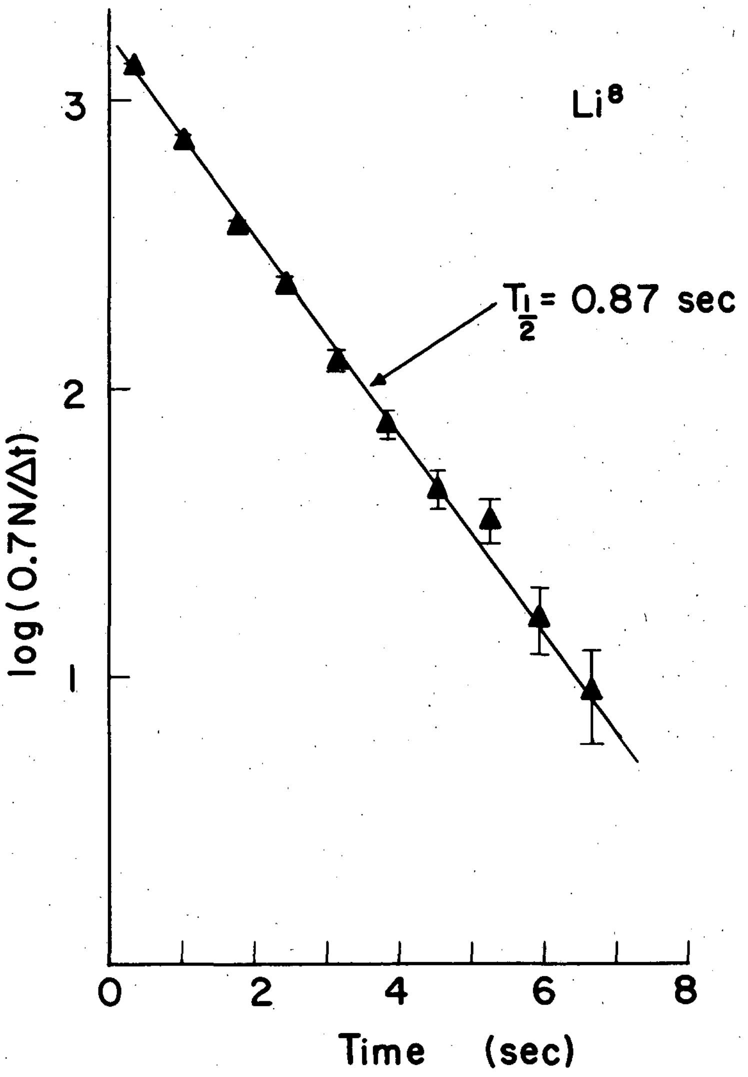

MU-15574

Fig. 12. Example of a decay curve for Li^8 (Run 4).

Table II

B^8 Lifetime

This experiment			Other experiments	
Run No.	Half life (sec)	Standard deviation	Half life (sec)	Reference No.
1	0.743	0.056	0.65 ± 0.1	3
2	0.812	0.046	0.61 ± 0.11	32
3 + 5	0.705	0.050	0.78 ± 0.01	36
4	0.736	0.048		
6	0.757	0.083		

Weighted mean of the half life is 0.75 ± 0.02 sec which includes an assumed 0.75% error in time scale.

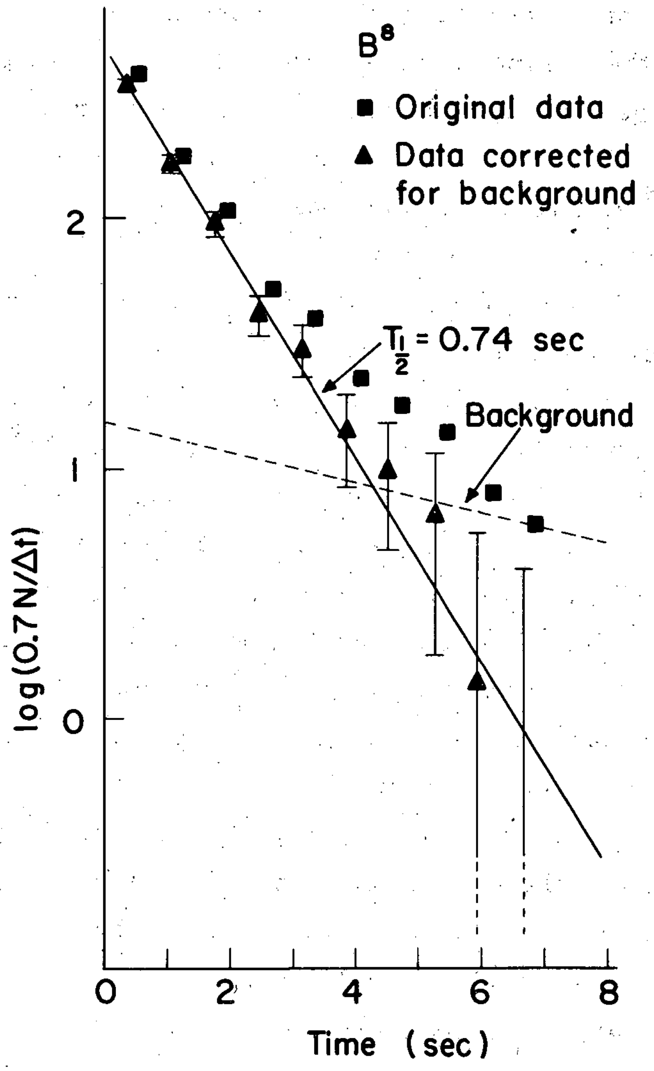

MU-15575

Fig. 13. Example of a decay curve for B^8 (Run 4). For clarity the background and original data are offset from the corrected data.

and the electron data were consistent with a half-life between 0.8 and 0.9 sec to as low as 1.5 Mev. These values are in agreement with the measured lifetimes. The identity is lost in the low-energy region in background and other activities. Most of the spectral data were then taken with the normal accelerator operation of 15 pulses per sec and a 50 msec gate delayed 12 msec after the beam pulse. The Kurie functions of the data taken by the two methods were in good agreement for both B^8 and Li^8, and indicate that there is little interference from other activities or background.

The data were corrected for scattering in the detector and for background. Because within statistical error the background was the same for B^8 and Li^8 above 15.5 Mev, the data were combined and fitted with a weighted least-squares line. For Li^8 in Channel A (Fig. 14) at 16 Mev, the background is about 0.3% of the peak spectral counts per microcoulomb, and at 7 Mev it is about 0.7%. For B^8 in Channel A (Fig. 15) the corresponding figures are 1.8% and 3.6%. In the figures, the Li^8 background appears much less than that for B^8 because of the normalization. The lifetime data taken above 15 Mev show no indication of any decay over a period of about 5 sec, but the counts in each gate are few.

The subsequent analysis of the Li^8 and B^8 beta spectra is complicated by the nature of the daughter nuclide Be^8.[37] This nucleus is unstable to heavy-particle emission, and the levels decay in a very short time into two alpha particles.

One approach would be to calculate the spectra by the use of the known data on the levels in Be^8. Because the states having the same angular momentum are widely spaced, one can apply the single-level resonance theory to obtain a density of states available to beta transitions.[38] Thus we have

$$a(E) = [E_0 - E)^2 + \Gamma^2/4]^{-1},$$

where E_0 is the excitation energy of the level and Γ is the full width at half-amplitude. Then a composite spectrum may be calculated if a superposition of many simple spectra each weighted by the corresponding a(E) is assumed. Using the first excited-state parameters,

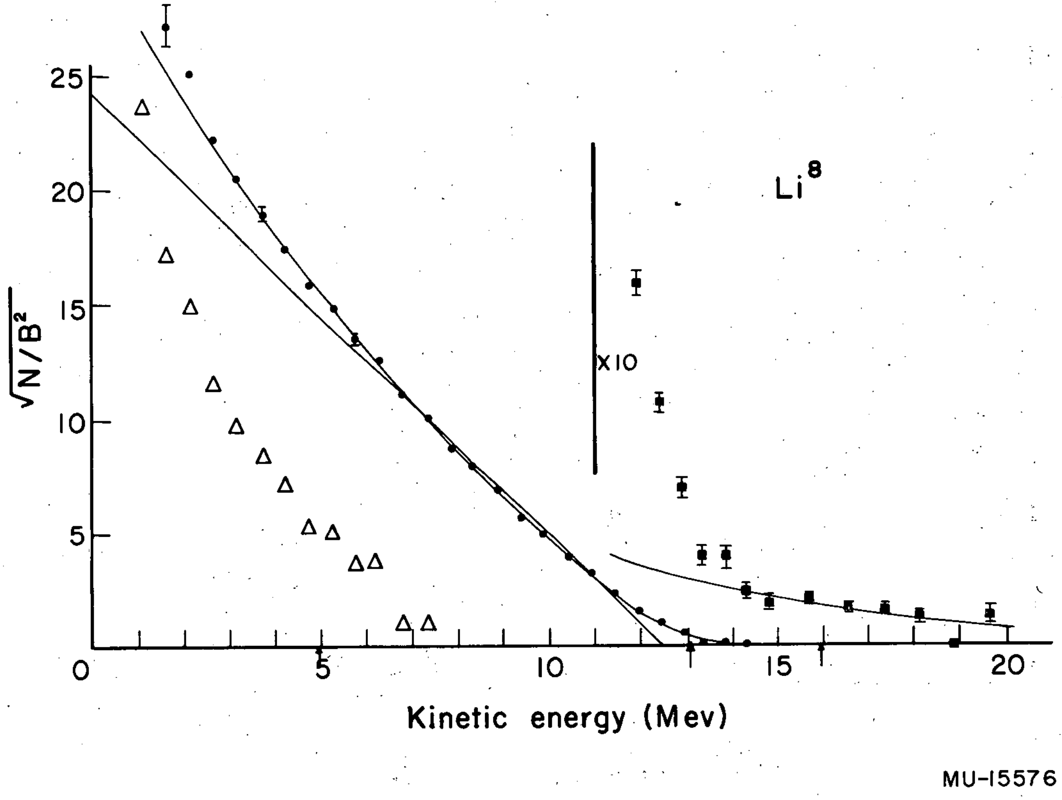

Fig. 14. Kurie function for Li^8 in Channel A. The end-point region is shown with an expanded ordinate and without the correction for background (dashed curve). The solid curve is calculated from the Be^8 alpha spectrum. The triangles are the branching obtained from the straight line. Standard deviations are indicated. The arrows indicate the expected end points for 0-, 2.9-, and 11-Mev levels in Be^8.

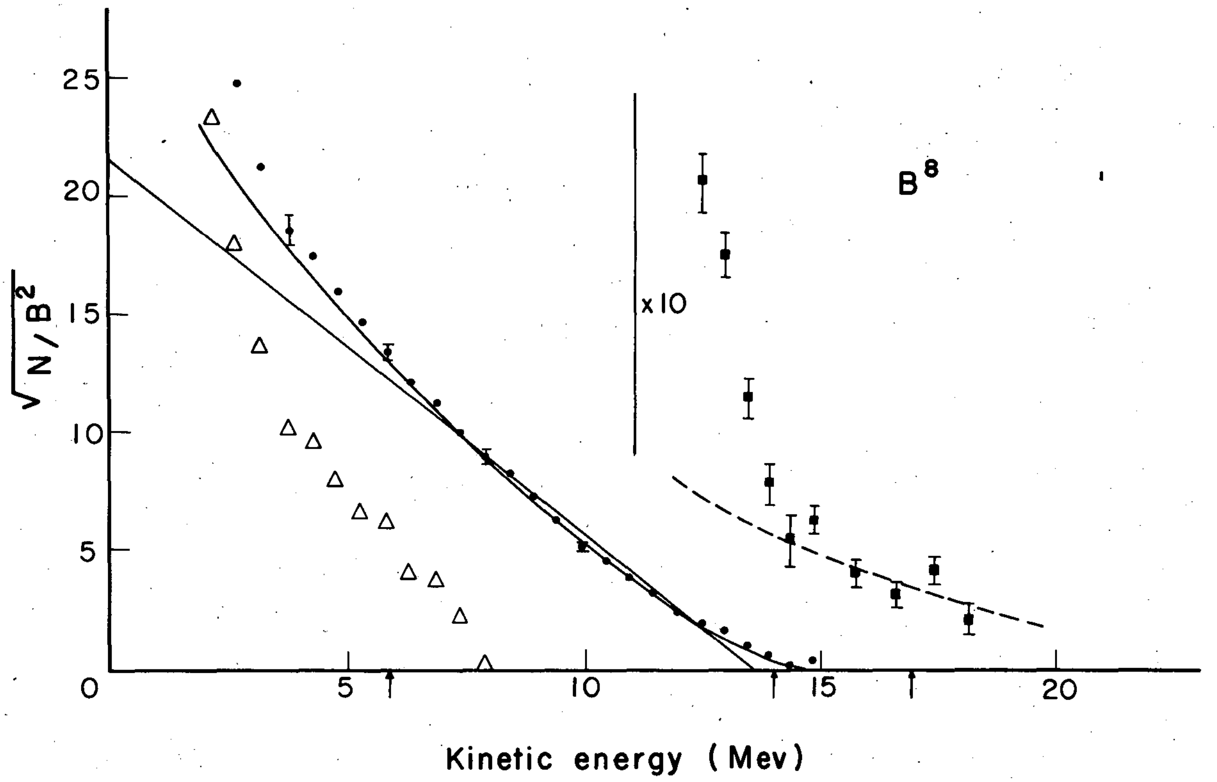

MU-15577

Fig. 15. Kurie function for B^8 in Channel A. The end-point region is shown with an expanded ordinate and without the correction for background (dashed curve). The solid curve is calculated from the Be^8 alpha spectrum. The triangles indicate the branching obtained from the straight line. Standard deviations are indicated. The arrows indicate the end points expected for 0-, 2.9-, and 11-Mev levels in Be^8.

one predicts an excess of high-energy electrons and a lack of low-energy ones. The Be^8 alpha spectrum predicted by this density of states if populated by the Li^8 decay is shown in Fig. 16. However, another factor, the Coulomb barrier to alpha decay,[39] has been neglected. Because in one mean life of the level following its creation by the beta transition, the electron travels a distance of the order of its wave length, the wave function of the electron and, as a result, its momentum may be affected by the Be^8 decay. The Coulomb barrier to alpha decay inhibits the transition from lower excitation energies more than from higher ones. Therefore one would expect fewer high-energy electrons than are predicted by the simple one-level theory. Incidentally, this does not explain the lack of transitions to the ground state, because the ground-state lifetime is much longer, and its decay should not perturb the electron wave functions. Multiplication of the one-level theory by the barrier-penetrability factor then gives one good agreement for the upper part of the beta spectrum. (Figure 16 shows the effect on the expected alpha spectrum). This factor is sensitive to the separation of the alpha particles in Be^8. A smaller radius increases the barrier and in consequence enhances the probability of lower-energy electrons relative to those at higher energy. This improves agreement with the data. But from the level width and from alpha-alpha scattering, one expects a fairly large separation of the alpha particles.[40] Therefore, to explain the low-energy electrons one must introduce transitions to higher levels in Be^8. There is strong evidence of a broad level near 11 Mev.[40] Here the Coulomb factor again inhibits the low-energy tail of the resonance, because the state has a short lifetime, and the barrier is higher because of the larger angular momentum.

Thus, to fit the beta spectra of Li^8 and B^8, one has several parameters for each level. These are the energy widths of the states, the alpha-particle separations, and the beta-decay transition probabilities to the two levels that depend on the angular momentum and nuclear configurations as well as the available phase space. Several combinations were tried, and it appears that a fit can be obtained with the 2.9-Mev and 11-Mev levels, but it seemed more enlightening to pursue other methods.

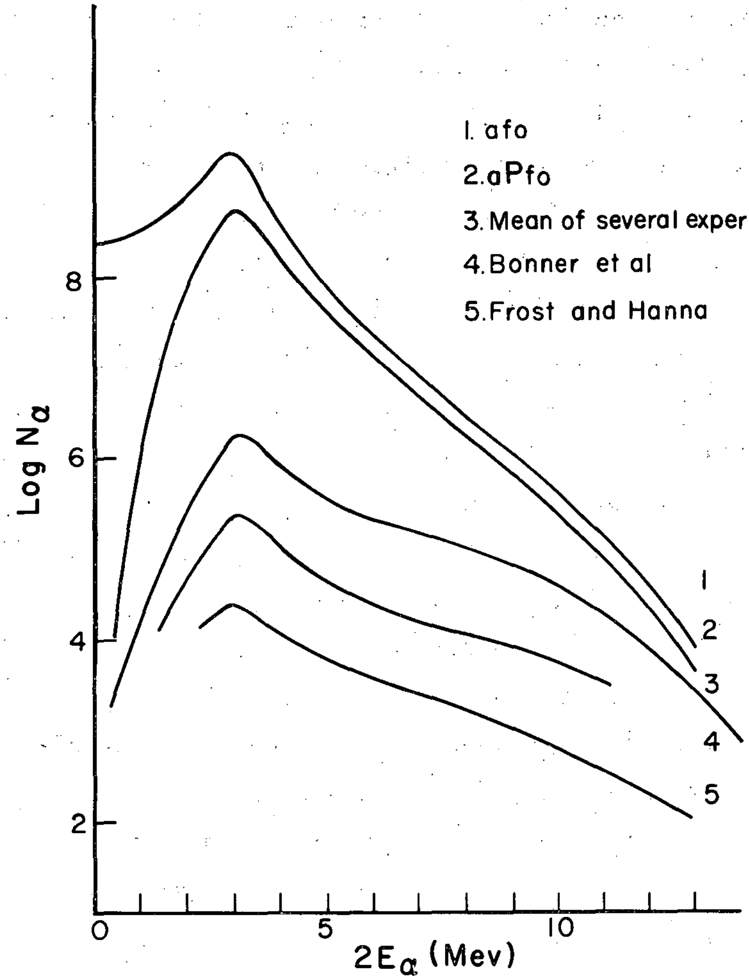

MU-15578

Fig. 16. Be^8 alpha spectra. Curve 1 is a one-level resonance distribution of states populated by the Li^8 beta decay. Curve 2 is modified by the Coulomb barrier to alpha decay of Be^8. Curve 3 is a mean from several experiments. Curves 4 and 5 are smooth curves through experimental data as presented by Frost and Hanna.

A second approach[41] is to correlate the complex spectral shapes with the experimental Be^8 alpha-decay spectra following the Li^8 transition[4, 42, 43] and the B^8 transition.[4] Gilbert finds that the alpha-decay following the Li^8 and B^8 beta transitions are the same within his statistics of 159 B^8 and 1252 Li^8 nuclei.[4] If one assumes no intermediate γ-ray transitions, the alpha spectrum should give the density of states in Be^8 available to beta transitions. But first an energy normalization must be made, because the beta-decay transition probability increases with the energy available. Let Q be the energy of the parent nuclide relative to the Be^8 ground state; then $Q' = Q + 0.096$ Mev is the energy available to the β-α cascade, because the ground state of Be^8 is unstable by 0.096 Mev.[37] Let $E' = 2E_\alpha$ be the total kinetic energy of the two alpha particles. Then the density of states $a(E')$ is given by

$$a(E')f_0(W_0) = a(E') \int_1^{Q''-E'} [(Q''-E')-W]^2[W^2-1]^{\frac{1}{2}} \, WdW = N_\alpha(E'),$$

where $N_\alpha(E')$ is the alpha spectrum, W the energy of the electron including its rest mass in units of m_0c^2, and

$$W_0 = Q'' - E' = Q' + 1 - E'$$

is the total energy available for the beta transition. In positron emission, two electron masses must be subtracted from the energy difference Q. The beta spectrum is given by

$$N(W)dW = F(Z, W)[W^2-1]^{\frac{1}{2}} Wd\,W \int_0^{Q''-W} a(E')[(Q''-E')-W]^2 \, dE'.$$

That is, at a given value of W there are contributions from all transitions with an upper energy limit $W_0 = Q''-E' > W$ each weighted by its corresponding $a(E')$.

Frost and Hanna present the measured alpha spectra of various experimenters.[42] From these an approximate mean curve (Fig. 16) is taken, and divided by the f_0 factor to obtain $a(E')$. Assuming $Q = 16.0$ Mev for Li^8 and $Q - 2m_0c^2 = 16.8$ Mev for B^8, one can calculate the Kurie functions expected.

Examination of the Kurie plot of the Li^8 data collected in Channel A (Fig. 14) and corrected for background and scattering but not for the energy shows good agreement above 3 Mev with the curve derived from the alpha spectrum. The calculated curve, which has been shifted slightly for a better fit, and the data are normalized arbitrarily at 7.35 Mev. Below 3 Mev one finds more electrons than predicted. The accuracy of the data collected in Channel B was statistically poorer. The calculated curve lies above the data from less than 4 Mev.

Both the electron data and alpha-particle data are inaccurate in this region. In the former, the scattering correction is large and the background uncertain. For the latter the numbers are small, being on the high-energy tail. One should note that Fig. 16 presents the logarithm of the alpha spectrum, and at first glance is misleading as to the actual number of high-energy alpha particles.

One can obtain a measure of the Li^8-Be^8 Q value from the fit of the Kurie function calculated from the alpha spectrum with Q = 16 Mev. If the curve is shifted 0.1 Mev to the left, one finds the closest fit. For Channel B a similar shift is needed. The accuracy is about 0.1 Mev and is partially dependent on the normalization. These values, corrected for the various effects mentioned in Section IV, 5 and 7, are recorded in Table III along with values from the literature. The mean value for Q is 15.94 ± 0.08 Mev. This gives a Li^8 mass excess of 24.97 ± 0.09 millimass units in agreement with accepted values.

Returning to the B^8 data, one finds a similar behavior. For Channel A, Fig. 15, the calculated Kurie function is in fair agreement with the data above 8 Mev. Below 6 Mev there is an excess of positrons over the predicted number. The percentage of background is higher than for Li^8 by a factor of five, and the extrapolation of the high-energy background may be insufficient. On the other hand, one may conclude that the excess of positrons indicates that transition to higher-energy Be^8 states is favored over the Li^8 transition more than is expected from the increased energy available. Also the

Table III

Q values for Li^8

Experiment	Q[a] (Mev)	Calibration correction to 13 Mev (Mev)	Ionization correction (Mev)	Resolution half-area correction (Mev)	Q (Mev)	Mass excess (mmu)	End point[b] (Mev)
This work:							
Channel A	15.9±.1	0.042±.026	0.02±.005	0.006±.003	15.97 ±.10		
Channel B	15.9±.1	-0.013±.032	0.02±.005	0.006±.003	15.91 ±.10		
Channels A and B						24.97±.09	
Other experiments:							
Reference 37						25.02±.03	
Weighted mean Q (Channels A and B)					15.94±.07 Mev		
With 0.3% calibration error (To 13 Mev)					15.94±.08 Mev =	17.12±.09 mmu	
							13.04±.08

[a] From fit of spectrum calculated from N_a.

[b] From 2.9-Mev level in Be^8.

$B^8(\beta^+)Be^8(2\alpha)$ alpha spectrum should show more high-energy alpha particles than the $Li^8(\beta^-)Be^8(2\alpha)$ spectrum. Gilbert finds the two alpha spectra the same, but his statistics for the B^8 cascade are insufficient to show up the 5 to 10% difference indicated by the beta spectrum.[4]

As before, one can obtain a Q value for the transition. No shifting of the calculated curve is needed for Channel A. For Channel B a shift to the right of 0.1 Mev improves the fit. Making the necessary energy corrections as before (Table IV), one obtains $Q = 17.91 \pm 0.12$ Mev, which gives a B^8 mass excess of 27.08 ± 0.13 millimass units. This is in good agreement with the listed values.

One can attempt to obtain branching percentages by subtracting out the successive components. Because no part of the Li^8 or B^8 spectrum shows linearity, one must draw a somewhat arbitrary straight line, with the result that any percentage of branching will be quite uncertain. On the other hand, by drawing a corresponding line for Li^8 and B^8 one can obtain qualitative numbers to compare the relative amounts of branching. Any transitions to the ground state are obscured by the background.

To begin, one can put upper limits on the decay to the ground state. The background counting rate increases as the focus energy decreases (Figs. 14 and 15). If one assumes a constant background determined by a mean value of the counts above the energy available for the ground-state transition and subtracts it from the data, an upper limit on the percent of decay can be obtained. This analysis indicates that less than 1% of the total Li^8 decay and less than 5% of the B^8 decay is to the ground state of Be^8. These limits are probably too high for several reasons. Firstly, the background was assumed flat, but actually increases toward lower energies. Secondly, the 2.9-Mev level of Be^8 is quite broad and, though the Coulomb barrier should inhibit the lower excitation-energy tail, the increased energy difference available to the beta transition counteracts this in part. Thus one may expect some electrons found in the region near the upper limit to belong to the transition to the first excited state. Another factor is that the lifetime data show no indication of a decay rate in this

Table IV

Values of Q and $Q-2m_0c^2$ for B^8

Experiment	$Q-2m_0c^2$ [a] (Mev)	Calibration correction to 14 Mev (Mev)	Ionization correction (Mev)	Resolution half-area correction (Mev)	$Q-2m_0c^2$ (Mev)	Mass excess (mmu)	Q (Mev)	End point[b] (Mev)
<u>This work</u>								
Channel A	16.8±.15	0.045±.028	0.02±.005	0.006±.003	16.87 ±.15			
Channel B	16.9±.15	-0.014±.035	0.02±.005	0.006±.003	16.91 ±.15			
Channels A & B						27.08±.13	17.91±.12	
<u>Other experiments</u>								
Reference 37						26.95±.30		
Reference 36						27.16±.01		
Reference 3						27		
		Weighted mean $Q-2m_0c^2$ (Channels A and B)			16.89±.11 Mev			
		With 0.3% calibration error (to 14 Mev)			16.89±.12 Mev			13.99±.12

[a] From fit of spectrum calculated from N_a.

[b] From 2.9-Mev level in Be^8.

energy range. Finally, the fact that the background is nearly the same for the various targets and activities indicates that these counts arise mainly from sources other than the target.

In the branching analysis of Li^8, an arbitrary line intercepting the abscissa at 12.5 Mev was fitted through the data near 7.5 Mev (Fig. 14). This gives a branching of about 11% to states above the 2.9-Mev level. It appears that a further separation into two components is possible with end points of about 7 and 3 Mev. But the end point of the higher-energy part depends on the straight line chosen previously. A reasonable fit to the data could be obtained from a transition to a broad level near 11 Mev.

Hornyak and Lauritsen find similar behavior for Li^8 with less than 2% transition to the ground state of Be^8 and about 10% to the 10 and 13-Mev levels;[2] Gilbert's combined alpha spectrum following the Li^8 and B^8 decay indicates about 15% from states above the 2.9-Mev level.[4]

For B^8 an analogous line (Fig. 15) is obtained by shifting the two fitted points up about 1 Mev, corresponding to the difference in the energy available for the beta transitions. This gives about 19% of the total to levels above 2.9 Mev. Again it appears possible to analyze the Kurie function into branches with end points of 4 and 8 Mev, or into one branch to a broad level near 11 Mev. Below 2 Mev there is a contribution due probably to an oxide film on the target.

The ratio of the Li^8 to B^8 produced by the 32-Mev protons is five to one, in agreement with Alvarez's findings.[3] One would expect the inverse with the B^8 from the p, 2n reaction more plentiful than the Li^8 from the p, 2p reaction.

This conclusion is based on the concept of the formation of a compound nucleus in the reaction. Because the energy of the incident proton is high and the atomic number of the target nucleus is low, the assumption of an intermediate nucleus probably is not valid. The predominance of the Li^8 activity may be explained by a p-p scattering process wherein the impinging proton is not bound and the other is knocked out of the nucleus. For emission of two neutrons, more complicated scattering mechanisms are required if one abandons the compound-nucleus idea. On this basis more Li^8 than B^8 is expected.

3. Conclusion

It appears that the Li^8 and B^8 spectra can be explained by transitions to the broad 2.9-Mev and 11-Mev levels of Be^8, on the basis of the shapes of the spectra and the prediction of these shapes from the alpha spectrum following the Be^8 breakup. Assuming these levels and the branching percentages, one may calculate the log-ft values. For Li^8 they are greater than 8 to the ground state, 5.67 to the 2.9-Mev level, and 4.6 to the 11-Mev level. The corresponding values for B^8 are greater than 7.3, 5.72, and 4.6.

The Li^8 and B^8 nuclides seem to be limited to spins of 2 or 3. Nordheim's rules for odd-odd nuclei predict either of these values.[44] The nature of the beta transition puts some restriction on the spin assignment. The ground state of Be^8 with spin zero is forbidden, and the 2.9-Mev level of spin 2 is allowed though unfavored for the decay as indicated by the ft values. This also suggests a spin of two or three for B^8 and Li^8. With the assumption that a single level is involved in the lower branch, the ft value is in the allowed range. From the agreement of the Kurie plot calculated from the alpha spectrum, one concludes that this level decays by alpha emission. Also a phase-shift analysis of α-α scattering indicates a spin-four level near 11 Mev.[40] Both the alpha-particle model[45] and shell model[46] predict a series of Be^8 levels of spin 0, 2, 4, ··· with nearly the proper ratio of energies. Other intermediate levels would require an excitation of the nucleus to levels outside the ground-state configuration, but no such calculations have been made. Recent experimental work, reviewed briefly by Nilson et al,[40] gives little support for the intermediate levels formerly reported. Therefore the evidence favors spin 3 for Li^8 and B^8 to permit allowed transitions to the spin-4 and spin-2 levels of Be^8 and not to the spin-zero ground state.

Some early evidence on angular correlations in the cascade from Li^8 indicated a forbidden transition.[33, 47] The conclusion is based on the assumption that no angular correlation exists for an allowed beta transition, but Morita and Yamada calculated possible angular dependences for allowed transition, assuming that p and d waves are effective at high beta-decay energies.[48] An improved experiment[49] which retracts earlier results[47] reports no angular correlation in the cascade.

B. Boron-12 and Nitrogen-12

1. Lifetime

The lifetimes of B^{12} and N^{12} were followed with consecutive gates covering up to 10 half lives with the linear accelerator operating at 7.5 and 3.75 pulses per second. Several sets of data were taken on different days, and the results for each nuclide were combined for an average half life.

The lifetimes from the least-squares fits to the B^{12} data are presented in Table V along with values from the literature. The mean value of the half life is 20.6 ± 0.2 msec, a figure falling between the older and newer values quoted. The second set of data is plotted in Fig. 17.

The N^{12} lifetime data are shown in Table VI. It was necessary to correct for a background in the last two runs. An assumed background (constant in time and of sufficient magnitude) was subtracted from the data to give a rough fit to a straight line on a semilog plot. Then the least-squares calculation was made. The other runs showed no need for a background correction. The mean value is 11.43 ± 0.05 msec and is lower than the 12.5 ± 1 msec reported by Alvarez.[7] Figure 6 shows the data for the third run.

2. Spectra

The data for the N^{12} and B^{12} spectra were collected with the normal 15 pulses-per-second repetition rate of the linear accelerator. With five tandem gates, each of 10-msec duration, the N^{12} activity could be followed for about five half lives between beam pulses, while B^{12} could be followed for about two and one-half. With this and other more extensive lifetime checks at various energies, the negative-electron spectrum was consistent with a lifetime of about 20 msec down to an energy of 2 Mev, where the counting statistics are poor. For N^{12} below about 10 Mev there is evidence of a small percentage of a longer-lived activity, and below 3.5 Mev the lifetime identity of N^{12} is obscured by other activities.

The background above the maximum energy of N^{12} was the same within statistics for N^{12} and B^{12} for both the thick and thin targets. Therefore all the data for each channel were combined to obtain better

Table V

B^{12} lifetime

This experiment			Other experiments	
Run No.	Half life (msec)	Standard deviation	Half life (msec)	Reference No.
1	21.19	0.57	22 ± 2	50
2	20.88	0.56	27 ± 2	51
3	20.91	0.79	27 ± 3	52
4	20.59	0.89	22 ± 1	34
5	20.71	0.67	$18.0^{+1.5}_{-1.3}$	53
6	21.16	1.14	18.5 ± 1	54
7	19.86	0.91		
8	20.12	0.40		
9	20.68	0.34		

Weighted mean half life (with assumed 0.3% error in time scale) = 20.6 ± 0.2 msec.

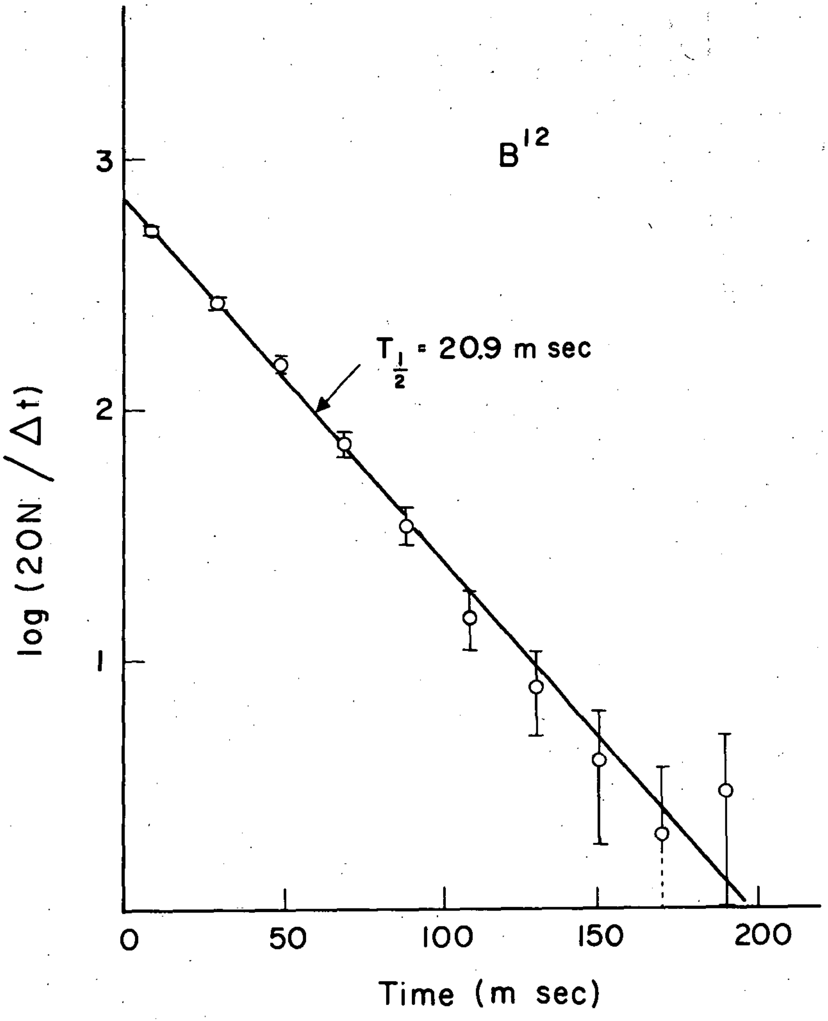

MU-15579

Fig. 17. Example of a decay curve for B^{12} (Run 2).

Table VI

N^{12} lifetime

This experiment			Other experiments	
Run No.	Half life (msec)	Standard deviation	Half life (msec)	Reference No.
1	11.492	0.086	12.5 ± 1	7
2	11.460	0.089		
3	11.576	0.101		
4	11.503	0.113		
5	11.360	0.046		
6	11.428	0.068		
Weighted mean half life (with assumed error in time scale of 0.3%) = 11.43 ± 0.05 msec).				

statistics for a least-squares straight-line fit. Channel A has a slightly higher background than B because of the modified detector slit. In Channel A this background at 16.5 Mev is 0.5% of the maximum counting rate. At the energy of the peak counting rate, the background is about 0.9%. For B^{12} the corresponding figures are 0.9% at 13.4 Mev and 1.2% at the peak counting-rate energy.

The Kurie function for B^{12} corrected for the extrapolation background and scattering is shown in Fig. 18. The energy has not been adjusted for the mean ionization loss in the target and the other energy corrections.

The end points of the spectrum were determined for the two targets and two detector systems by least-squares straight lines through the data above the first branch. Table VII contains the four values and the energy corrections. The mean value is 13.40 ± 0.05 Mev, which gives a B^{12} mass excess of 18.19 ± 0.06 millimass units, in agreement with the other values given.

One component to the 4.43-Mev C^{12} level can be resolved,[37] but the scatter of the data does not permit any further separation. The four sets of data do indicate that one and possibly two other states are involved. The relative amounts of the transitions to the ground state and first excited state are 100 to 6 with log-ft values of 4.11 and 4.5. The remainder is a few percent of the total. Hornyak and Lauritsen analyze their B^{12} spectrum (see Fig. 18) into the ground-state component, with 5% to the 7.65-Mev level, and a level or levels near 11 Mev in C^{12}.[2] They state that up to 5% decay to the 4.43-Mev level cannot be excluded. Tanner, using least-squares methods, reanalyzed Hornyak and Lauritsen's data with the benefit of recent data on C^{12} levels.[5] He obtained a good fit with less than 0.1% to the 4.43-Mev level, 4.8% to the 7.65-Mev level and 3.2% to a level near 11 Mev. However, the plot versus total energy of the function $[N/p^2]^{\frac{1}{2}}/[W_0-W]$ shows up to 2% to the 4.43 Mev-level and several percent to the 9.61-Mev level.

Then, studying β-γ and γ-γ coincidences from the B^{12} decay, Tanner found, relative to the transition to the C^{12} ground state, 1.7 ± 0.4% to the 4.43-Mev state and 0.0 ± 0.2% to the 7.65-Mev level

Table VII

B^{12} end point

Experiment	Target	Least-squares end point (Mev)	Calibration correction (Mev)	Ionization correction (Mev)	Resolution half-area correction (Mev)	End point (Mev)	Mass excess (mmu)
<u>This work</u>							
Channel A	Thick	13.296±.045	0.040±.027	0.095±.02	0.006±.003	13.437±.056	
Channel A	Thin	13.272±.085	0.040±.027	0.05 ±.01	0.006±.003	13.368±.090	
Channel B	Thick	13.253±.033	-0.013±.033	0.095±.02	0.006±.003	13.341±.051	
Channel B	Thin	13.484±.095	-0.013±.033	0.05 ±.01	0.006±.003	13.527±.101	
Channels A & B							18.19±.06[a]
<u>Other Experiments</u>:							
Reference 2						13.43±.06	18.22±.06
Reference 37							18.163±.021

Weighted-mean end point (Channels A & B)	13.397±.035 Mev
With 0.3% calibration error	13.40 ±.05 Mev
Q value	13.40 ±.05 Mev = 14.39±.06 mmu

[a] The mass excess of C^{12} is 3.804 ± .016 mmu.[37]

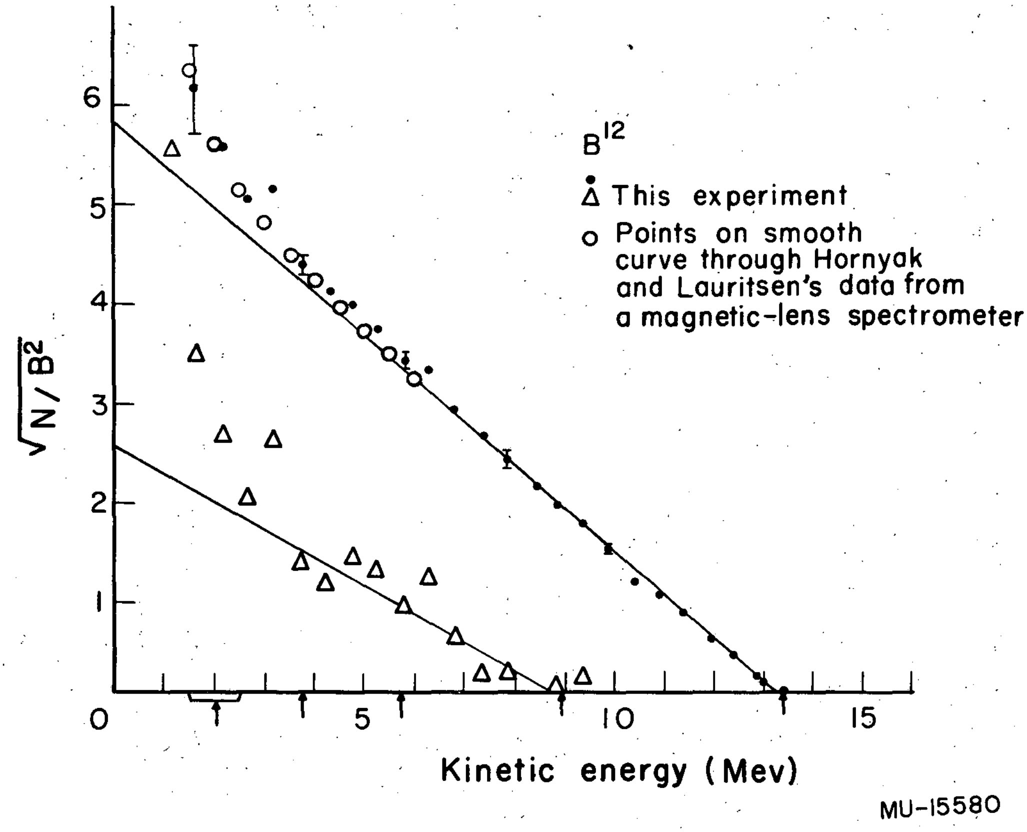

Fig. 18. Kurie function for B^{12} in Channel A with the thick target. The curve from a magnetic-lens spectrometer is also presented. The arrows indicate the end points expected for the C^{12} levels. These are not shifted to account for the energy losses and calibration corrections.

if that level decays by a cascade only.[5] Cook et al., by detection of alpha particles associated with the B^{12} beta transition, find that 1.3 ± 0.4% of the total decay is to the 7.65-Mev level of C^{12}, which then decays primarily into alpha particles.[6] It seems then that the present data give too large a branching percentage to the 4.43-Mev level, but this figure may be in error by 50%.

As mentioned previously, the N^{12} spectrum is accompanied by other activities. Using the lifetime data collected with the spectral measurement, one can obtain a background in addition to that determined by the extrapolation of the counts above the maximum energy. The procedure is to subtract a background that is constant in time from the data in the five gates to obtain a fit to an 11.5-msec half life. This was done for the thick target, which has better counting statistics. The background numbers obtained fluctuate quite a bit, but show a decrease with increasing energy. A smooth curve was drawn through the data and joined to the straight-line background at about 12 Mev. There is a sharp rise at about 3.5 Mev due to another activity.

The higher-energy part of this additional background is probably B^8. Alvarez,[3] in proton bombardment of a CH_4 proportional counter, observed a weak delayed alpha emitter of about a 0.5 sec half life and a threshold consistent with the $C^{12}(p, n\alpha)B^8$ reaction.

Assuming that the added background is B^8, one finds that the total amount of B^8 is less than 2% of the total N^{12} decay in the five gates for the thick target and a repetition rate of 15 pulses per second. One can calculate the expected shapes of the Kurie function for each of the five gates with small percentages of B^8 and compare them with the actual data. The shapes are quite different toward the lower energies, because the amount of N^{12} decreases by a factor of 11 over five 10-msec gates while the B^8 contribution is nearly constant. The actual data from the first through the fourth gates seem to agree in shape fairly well with one another. The Kurie function from the fifth gate indicates some B^8, but the statistics are poor. The five Kurie functions were normalized by the least-squares line through the data above 12 Mev, and the agreement is partially dependent on this normalization. It appears that an upper limit of about 2% of the number of positrons detected are from B^8 for this target and proton pulse rate.

The steep rise in the activity below about 3.5 Mev seems to originate from the C^{13}, because polyethylene targets do not show it. As a result of the reduction from $BaCO_3$ with magnesium and the subsequent washing with hydrochloric acid, there may be several impurities in the C^{13} that could give rise to positron activities in this region.

The Kurie function for N^{12} is shown in Fig. 19. The background from the decay curves and that extrapolated from above the maximum energy have been subtracted and the scattering correction applied. The data have not been adjusted for the mean ionization loss and the other energy corrections. Because of the uncertainty in the background, the data below 3 Mev are not presented.

To determine the end point of the spectrum, a least-squares straight line was fitted to the points above the first branch for the thick and thin targets and the two detector channels. These values and the energy corrections are presented in Table VIII. The mean end point is 16.37 ± 0.06 Mev, which gives a mass excess of 22.48 ± 0.06 millimass units. This agrees with the value obtained by Ajzenberg-Selove et al.,[55] but is less than Alvarez's value by several standard deviations.[7]

Two branches may be resolved in the Kurie function. The straight lines shown are fitted to the data and to the end points corresponding to the 4.43-Mev and 7.65-Mev levels in C^{12}. The mean energy loss in the target and the calibration adjustments have been subtracted to agree with the energy scale of the graph. For the three components, the lines give relative amounts of 100, 15, and 3 with log ft values of 4.17, 4.4, and 4.4. Alvarez, in studying delayed alpha emitters, found an activity consistent with an N^{12} transition to a level of C^{12} near 11 Mev, which decays into three alpha particles.[3] This branch could be easily masked in the experiment reported here by the large background subtraction in this energy region.

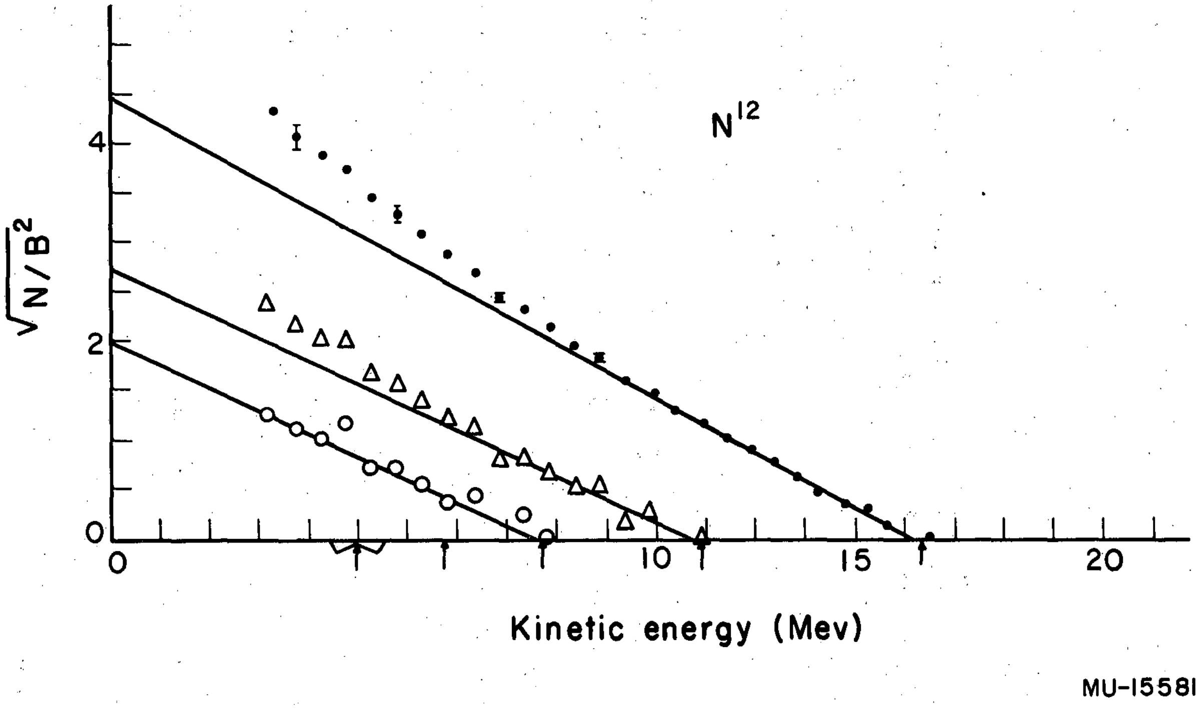

Fig. 19. Kurie function for N^{12} in Channel A with the thick target. Below 3 Mev the N^{12} is obscured by other activities. The arrows indicate the end points expected for the C^{12} levels. These are not adjusted for the energy losses and calibration corrections.

Table VIII

Nitrogen-12 end point

Experiment	Target	Least-squares end point (Mev)	Calibration correction (Mev)	Ionization correction (Mev)	Resolution half-area correction (Mev)	End point (Mev)	Mass excess (mmu)
This work							
Channel A	Thick	16.260±.053	0.049±.032	0.095±.02	0.007±.003	16.411±.065	
Channel A	Thin	16.255±.043	0.049±.032	0.05 ±.01	0.007±.003	16.361±.055	
Channel B	Thick	16.209±.070	-0.016±.041	0.095±.02	0.007±.003	16.295±.084	
Channel B	Thin	16.347±.051	-0.016±.041	0.05 ±.01	0.007±.003	16.388±.066	
Channels A & B							22.48±.06[a]
Other experiments							
Reference 7						16.6 ±.2	22.8 ±.15
Reference 55							22.55±.07
			Weighted mean end point (Channels A and B)			16.370±.032 Mev	
			With 0.3% calibration correction			16.37 ±.06 Mev	
			Q value			17.39±.06 Mev = 18.68±.06 mmu	

[a] The mass excess of C^{12} is 3.804±.016 mmu.[37]

3. Conclusion

The evidence from this experiment and the several others mentioned shows that the N^{12} and B^{12} nuclides decay, as expected, to the same levels in C^{12}. The log-ft values and the spins of the C^{12} states favor a spin of 1 for these mirror isotopes. The shell-model rules for odd-odd nuclei also predict this spin.[44]

VI. ERRORS

A. Energy Calibration

In reduction of the data it was assumed that the current-versus-energy calibration was within 0.3% of absolute. This estimate arises from three factors: the error in calibration of the bismuth magneto-resistance fluxmeter,[56] the error in radial distances, and the error in the setting and drift of the excitation currents. If all the magnetic field values are too high or too low by the same percentage, the focus energy is in error by this same percentage.

A bismuth fluxmeter calibrated against nuclear magnetic resonance equipment manufactured by the Laboratory for Electronics was used to measure the radial magnetic-field distribution in the median plane. The resistance of the bismuth probe, heated and temperature-regulated to ± 0.04°C, was measured in a Wheatstone bridge circuit to within less than 0.1%. The gradient of the magnetic field in the region of probe calibration was less than 0.1%. The drift of the excitation current, which was monitored by the nuclear resonance during the radial runs, was less than 0.1% and could be corrected in the calculations. Other contributing factors are temperature fluctuations in the heated probe and the finite dimensions of the bismuth coil. The latter introduces errors in regions of large or changing field gradients. The combined error from all these causes is about 0.2%.

The measurement of the radius introduces another error. The bismuth probe was driven by a worm gear and crank with a relative accuracy of about ± 0.004 in. at any radius over the 10-in. range. A larger error results from the determination of the magnetic axis. This is located by the minimum of the magnetic field to within 0.01 in. The calculated energy is in error by 0.15% for this error in the radius.

The current-setting error is a result of several factors. The dial on the potentiometer can be set to within less than 0.05% for energies above 5 Mev. The current can be adjusted to the potentiometer setting to about 0.1% accuracy. If there is a slight overshoot in setting the current, the hysteresis of the magnet introduces an error of about 0.1% in the field when the current is reduced to the proper value.

The current drift is less than 0.1% and is caused mainly by temperature changes in the coils as different currents are set. The combined error from these causes is about 0.2%. This is verified by the current settings in the calibration runs, in which a little more care was taken than during the actual measurements of the spectra. At a current setting for about 15-Mev electrons and with the field monitored by the nuclear resonance, the reproducibility in the magnetic field was about 0.1% for nine repetitions; at about 7 Mev it was 0.14%.

In conclusion, then, the combination of these three groups of errors gives a calibration of current against magnetic field and focus energy within 0.3% of absolute, above 10 Mev.

Because of a slight horizontal misalignment of the axes of the two poles of the magnet, the radial magnetic-field distribution is not symmetric. The energy-calibration curve was determined from field measurements on the A side in the horizontal plane. The focus energy on the B side is 0.54 ± 0.05 % less than the A side for the same current setting.

There is another adjustment necessary because the slit systems were nominally centered on a radius of 7.75 in., a focus-orbit value obtained from preliminary field measurements. The radial distances to the centers of the slits were slightly larger when measured. The more accurate magnetic measurements following the experiment gave a value of 7.71 in. for the focal circle. For a measure of the energy shift needed, one detector system was raised radially 1/8 in., and the apparent decrease in the N^{12} end point was 0.12 ± 0.06 Mev. Assuming a linear shift in energy as the detector is moved radially, one computes for Channel A an energy correction of 0.32 ± 0.19 % to be added to the calibration curve. For Channel B, 0.45 ± 0.25 % must be added. The quoted errors include the accuracy of the measurement of the radii and the 0.01-in. reproducibility figure for detector replacement.

The possibility of a change of the spectrometer line shape with a shift in detector position should be considered. Any change would displace the half-area line (Section IV, D7) and require a different energy correction for the asymmetry. But results of studies on the line shape of a monoenergetic plutonium alpha-particle source in a 40-in. spiral-orbit spectrometer indicate that the shape does not change significantly with small radial displacements of the detector. It is assumed not to change in the geometry that was used in this experiment.

Thus there are small corrections to the calibration curve for the detector positions and the field asymmetry. For Channel A the first effect requires an increase of 0.3 ± 0.2 % in the energy from the calibration curve. For Channel B the combination of the two effects requires a decrease of 0.1 ± 0.25 %.

B. Magnetic Saturation

One factor that must be studied carefully in this type of spectrometer is magnetic saturation of the pole pieces. Because the focal circle is just outside the core radius, any nonuniformity in the magnetization of the iron could seriously affect the detection efficiency as the current is increased. For finding such effects, careful field measurements were made to radii of 10 in. For seven energies between 6 and 17 Mev, the radial field values normalized by the maximum field for the particular energy were compared at every 0.5 in. The maximum root-mean-square deviation from the mean out to 7.5 in. was about 0.3% for the field at any particular radius. No energy-dependent trend was noticed in the data, but it would be expected for nonuniform saturation. Therefore, within the accuracy of the measurements, no effects from this cause are present.

C. Energy Loss in the First Geiger Tube

A correction is possibly needed for the energy loss of the electrons in traversing the first Geiger tube. The most probable loss is about 0.1 Mev. The momentum loss would result in a different radius of curvature, and electrons otherwise detected might miss the final Geiger tubes. This effect would lower the apparent energy measured.

In order to test this effect 0.020 and 0.040 in. of aluminum equivalent to about two and four times the tube thickness were placed in turn after the first tube, and spectral points were measured near the N^{12} end point. Unfortunately the scattering caused by the added material masks the effect. Conflicting results are obtained in reducing the data by various extrapolations of the scattering correction. It seems likely that the correction is less than 0.02 Mev at 16 Mev.

Because the most probable energy loss is nearly constant down to a few Mev, the effect becomes larger at lower energies. Because of the lack of knowledge on this effect, no corrections have been made to the spectral data.

D. Misalignment

Another effect that may cause error in the energy measured is target and collimator misalignment with respect to the magnetic axis. The upstream axial hole centers the collimator, while the downstream hole centers the target. Before the experiment the axial holes were misaligned by about 0.05 in. By shimming of the yoke, the alignment was improved. Measurements with a transit indicated that the misalignment of the axial holes was about 0.01 in. Thus the target and collimator could be off as much as 0.01 in. relative to the magnetic axis. An experimental study of the shift of the N^{12} end point was made with a 1/8-in. collimator which was 1/16 in. off center. In one case it was set horizontally nearer the detector and in another vertically down from the axis. The upper limit apparently increases by 0.06 ± 0.06 Mev. For the opposing positions, because of the longer path in the central field region, a lower energy should be measured. Therefore a misalignment of 0.010 in. would require an energy correction of less than 0.1%. This has been neglected in the data reduction.

E. Drifts

As mentioned before, the effect of drifts seems to be small (Section IV, D2). Small variations in the magnet current would not show up in the external-to-internal consistency ratio of the counts at the normalization point, since the spectra are relatively flat there. For higher or lower energies there would be a change in counting rate. The monitoring of the excitation current indicated that this drift was less than 0.1%. Some change might appear at higher and lower energies, but with the drifts of less than 0.1% any change in counting rate would be within the counting statistics. Occasional scaler malfunctioning causes errors, but usually for such cases the data are obviously in error and can be thrown out.

Fluctuations in the proton beam also cause drifts, but they are quite limited. Shifts of the center of the proton current density in the target and changes in proton energy because of fluctuations in the accelerating mechanism of the linear accelerator and also drifts in the steering-magnet current, cause variations in counting rates. These variations are due to the excitation functions of the activities and to different background, which depend on the proton energy and distribution in the target. Only small fluctuations would be passed by the collimators without a total beam loss. The general background level changes as more beam is lost at the collimators. Changes in intensity of the beam current change the background as well as dead-time losses. During most of the runs the beam was fairly steady, and checks using various beam intensities gave the same counting rates within the statistical limits of the data.

Other fluctuations arising from beam monitoring and the electronics are small, as indicated by the consistency of the data at the normalization points.

VII. CONCLUSIONS

The results turn out to be as expected. The transition of the mirror pairs involves the same levels of the daughter nuclides. The lifetimes and end points are in fair agreement with published data.

There are several improvements that could be made in the experiment, especially in the detector system. Construction of thin-walled proportional counters would help in several ways. The faster resolving times permit higher counting rates. The sensitive area could be restricted to about the slit size of the detector system to reduce background. With thinner walls and perhaps two or three counters inside one container the scattering problem could be reduced appreciably. Centering the slits in the focal circle would improve the accuracy of the energy determinations. It might also improve the signal-to-noise ratio. There should be an increase in transmission as the detector is moved inward, and the background should remain about the same if it comes mainly from sources other than the target.

For studying the branching percentages and energies an obvious improvement would be the detection of β-γ and β-α coincidences. With the large transmission of the spectrometer this would be quite feasible.

In part, the experiment is a demonstration of the spiral-orbit spectrometer. One can obtain high transmission and still have fair resolution because of the unique focusing features of the instrument. The agreement of the measured end points with values in the literature shows that the insturment can be accurately calibrated with only the theory as a guide. Another evaluation of a spectrometer is to compare its spectral shapes with those obtained by other instruments. The B^{12} spectrum has been measured in a ring-focus magnetic-lens spectrometer.[2] Figure 17 shows points from a smooth curve drawn through the data. Above 6 Mev it is a straight line. Within the statistical errors, the shape obtained by the spiral-orbit spectrometer is the same. A slight change in normalization could possibly improve the agreement. The main limitation on the accuracy of this particular spectrometer in the low-energy regions is the detector system, but there is much room for improvement here.

There are several advantages associated with this type of spectrometer in use with particle accelerators. Normally the beam is brought down the axial hole, and changes in the magnetic field do not deflect it as in the uniform-field 180-deg spectrometer. The iron and the current coils provide good shielding for the detectors from background radiation from the accelerator. Often it is desirable to detect particles of both charges, as in meson production, and for this a spiral-orbit spectrometer is quite suitable.

For sources of low activity, the high transmission by this type of focusing is advantageous. With some sacrifice in resolution the detection probability can be greatly increased by making several modifications. Use of larger counters, both radially and in the z direction, and a wider annular slit will increase the counting rate. A field distribution with a smaller gradient near the focal circle and extending inward to smaller radii will decrease the radial dispersion of trajectories near the focal orbit and also increase the z -focusing properties of the field. Both serve to increase the counting rate. Finally a reduction in the central angle subtended by the detector slit system will increase the counting rate.

VIII. ACKNOWLEDGMENTS

The author is indebted to the following individuals for aid and encouragement during this project:

To Dr. Walter H. Barkas, who suggested the problem and offered many helpful suggestions; to Dr. Robert Thornton for his interest; and to Dr. Ryokichi Sagane for his suggestions and discussions on the spiral-orbit spectrometer.

To Dr. Edward Gross and Dr. Edwin Iloff for aid in the preliminary stages of the experiment, and to Dr. Walter Dudziak for assistance in the completion of the experiment.

To the linear accelerator crew under Mr. James Sirois for help when needed and for the steady operation of the machine; to the magnetic measurements group for the use of their equipment and knowledge; to Mr. Norris Nickols for occasional relief during the data-collecting routine.

To the electronics group for maintaining the counting circuits in good repair.

To Dr. Bert M. Tolbert for kindly supplying the C^{13}-enriched $BaCO_3$, and to Mr. Albert Salo for the reduction to C^{13}.

To Elizabeth Geran Vedder for encouragement and for typing the manuscript.

To the many others who gave their assistance to make the effort easier.

This work was performed under the auspices of the U. S. Atomic Energy Commission.

IX. APPENDICES

A. Theory of the Spiral-Orbit Spectormeter

For a magnetic field axially symmetric around the z axis, with $z = 0$ a plane of symmetry, the components of the magnetic field in cylindrical coordinates (r, θ, z) satisfy the following conditions:

$$H_r = H_r(z, r) = -H_r(-z, r)$$

$$H_\theta = 0$$

$$H_z = H_z(z, r) = H_z(-z, r).$$

The vector potential A is helpful in this case, its components being $A_r = A_z = 0$ and $A_\theta = A_\theta(r, z) = A$, where $H_r = -\frac{\partial A}{\partial z}$, $H_\theta = 0$ $H_z = \frac{1}{r} \frac{\partial}{\partial r} (rA)$. For a particle of charge e and mass m, the relativistically valid equation of motion is

$$\dot{\vec{p}} = e \, \dot{\vec{r}} \times \vec{H}.$$

Expressed in terms of its three components, it is

$$m(\ddot{r} - r\dot{\theta}^2) = e r \dot{\theta} \, H_z = e \dot{\theta} \frac{\partial}{\partial r} (rA), \tag{1}$$

$$m(r\ddot{\theta} + 2\dot{r}\dot{\theta}) = -e\dot{r} H_z + e\dot{z} H_r = -\frac{e}{r} \frac{d}{dt} (rA) \tag{2}$$

and

$$m\ddot{z} = -e r \dot{\theta} H_r = e r \dot{\theta} \frac{\partial A}{\partial z}. \tag{3}$$

Equation (2) may be rewritten as

$$m \frac{d}{dt} (r^2 \dot{\theta}) = -e \frac{d}{dt} (rA).$$

By integration, we find

$$r\dot{\theta} = -\frac{e}{m} [A + \frac{C}{r}]. \tag{4}$$

For initial conditions, we have

$r = r_0$, $A = A_0$, $\dot{\theta} = \dot{\theta}_0$, and $-C = \frac{m}{e} r_0^2 \dot{\theta}_0 + r_0 A_0$. Now substituting the expression for $r\dot{\theta}$ of Eq. (4) in $v^2 = \dot{r}^2 + \dot{z}^2 + (r\dot{\theta})^2$, we obtain

$$\dot{r}^2 + \dot{z}^2 = v^2 - (\frac{e}{m})^2 [A + \frac{C}{r}]^2. \tag{5}$$

For a particle starting from the center and moving in the plane of symmetry, we have $C = 0$, $z = 0$, $\dot{z} = 0$, and

$$\dot{r}^2 = v^2 - (e/m)^2 A^2 \tag{6}$$

and

$$mr\dot{\theta} = -eA. \tag{7}$$

For a spiral orbit approaching a circle of radius $r = \rho$, the conditions at $r = \rho$ must be $\dot{r} = 0$, $\ddot{r} = 0$. Substituting the former equation into Eq. (6) and using Eq. (7), we obtain

$$mv = -eA(\rho) = m\rho\dot{\theta}. \tag{8}$$

Substituting the latter conditions in Eq. (1) and using Eq. (7), we find

$$-m\rho\dot{\theta} = +e\rho H_z(\rho) = eA(\rho). \tag{9}$$

Applying Stokes's theorem, $\phi = \oint \vec{A}\cdot d\vec{l} = \int_s \vec{\nabla}\times\vec{A}\cdot d\vec{s} = \int_s \vec{H}\cdot d\vec{s}$, we obtain

$$A(\rho) = \frac{1}{\rho}\int_0^\rho H_z\, r\, dr$$

and, therefore,

$$A(\rho) = \rho\, H_z(\rho) = \frac{1}{\rho}\int_0^\rho H_z(r)\, r dr. \tag{10}$$

Using Eq. (9) and $H_z = (1/r)\frac{\partial}{\partial r}(rA)$, we find

$$\left(\frac{\partial A}{\partial r}\right)_\rho = 0, \tag{11}$$

and thus the vector potential is a maximum at $r = \rho$. From Eqs. (8) and (10) the momentum of particle in the orbit and the radius of the orbit are determined. One should note that the position of this orbit is not affected by the absolute value of the magnetic field but only by the shape of the distribution. The value of ρ is quickly found by plotting $H\cdot r$ and $A(r)$ and locating their intersection, which determines ρ, Fig. 4. The vector potential may be found from $H\cdot r$ by Simpson's Rule[57] or by integration of curves fitted to the field values. With the latter method, ρ can be determined from Eq. (11).

A trajectory in the median plane may be determined from

$$\theta = \int_{r_0}^{r} d\theta = \int_{r_0}^{r} \frac{\dot{\theta}}{\dot{r}}\, dr, \tag{12}$$

where $\dot{r}$ and $\dot{\theta}$ are obtained from Eqs. (4) and (5) with $\dot{z} = 0$.

In any practical case the source and detector have finite dimensions, and one must determine the intensity and resolution of the spectrometer. To derive the line shape or resolution function, consider in the median plane the homogeneous emission in all directions of monoenergetic charged particles from the cylinder of radius r_0 centered on the magnetic axis. Let the center of the detector of radial width 2d be on the focal circle. Then, using Eq. (12), one can calculate the probability of detection defined as $I = \Theta/2\pi$, where Θ is the central angle for which the trajectory falls between the two concentric circles $\rho + d$ and $\rho - d$. For Θ larger than 2π, the intensity should be taken as one. This is the physical restriction by the detector which permits a maximum of one revolution of the particle in the region of the focal circle.

Let $A(\rho) = D$ with $A'(r)$ and $A'(\rho) = D'$ designating values for a different magnetic-field intensity. Then, substituting Eqs. (4) and (5) into Eq. (12), we have

$$\Theta = \int d\theta = \int \frac{d\theta}{dr}\, dr = \int_{\rho - d \leq r \leq \rho + d} \frac{e}{m}\left(\frac{A'}{r} + \frac{C}{r^2}\right)\left[v^2 - \left(\frac{e}{m}\right)^2 \left(A' + \frac{C}{r}\right)^2\right]^{-\frac{1}{2}} dr .$$

In the neighborhood of the focal circle, we may expand $A(r)$ in a Taylor's series thus

$$A(r) = A(\rho) - (\rho - r)\left(\frac{\partial A}{\partial r}\right)_\rho + \frac{(\rho - r)^2}{2}\left(\frac{\partial^2 A}{\partial r^2}\right)_\rho + \cdots .$$

But $\partial A/\partial r$ equals 0 at the focal radius, and division by $A(\rho)$ gives

$$A(r)/A(\rho) = 1 - (1-x)^2/\kappa^2 ,$$

where $x = r/\rho$ and $\kappa^2 = -2A(\rho)/\left[\rho^2 \left(\frac{\partial^2 A}{\partial r^2}\right)_\rho\right]$. In more familiar terms: assuming $H = H(\rho)(\rho/r)^n$ near ρ, we find $\kappa^2 = 2/(n-1)$. In this region n is greater than unity and usually about 3.

For particles starting close to the axis, $r_0 A_0$ is negligible. Therefore we have

$$-C = (m/e) r_0^2\, \dot{\theta}_0 = r_0 v \sin\alpha = A(\rho) r_0 \sin\alpha ,$$

where α is the angle between the direction of emission and a radius through the point of emission. Also for r close to ρ, C/r^2 can be neglected to give

$$(e/m)[A'/r + C/r^2] \simeq (e/m)(D/\rho)$$

and

$$\begin{aligned} v^2-(e/m)^2(A'+C/r)^2 &= \{v+(e/m)(A'+C/r)\}\{v-(e/m)(A'+C/r)\} \\ &\simeq (e/m)^2(D+D')\{D-D'[1-(1-x)^2/\kappa^2]-C/r\} \\ &\simeq (e/m)^2\,2D^2\}(x-1)^2/\kappa^2-\Delta D/D-(r_0/r)\sin\alpha\}. \end{aligned}$$

Then we have

$$\Theta = \int \frac{\kappa}{\sqrt{2}}\left[(x-1)^2-(\Delta D/D)\kappa^2-(r_0/\rho)\kappa^2\sin\alpha\right]^{-\frac{1}{2}}\,dx,$$

$$1-d/\rho \le r/\rho \le 1+d/\rho$$

or

$$\Theta = \int (\kappa/\sqrt{2})\,[y^2-(\Delta D/D)\kappa^2-(r_0/\rho)\kappa^2\sin\alpha]^{-\frac{1}{2}}\,dy,$$

$$-\delta \le y \le \delta$$

where

$$\delta = d/\rho,\quad y = x-1 = (r/\rho)-1\ .$$

There are two cases to consider:

(a.) $\Delta D/D + (r_0/\rho)\sin\alpha > 0$.

Here we have

$$y \ge [\Delta D/D+(r_0/\rho)\sin\alpha]^{\frac{1}{2}} \equiv y_0$$

and the particles reach $1-y_0$ before turning back. Thus we have

$$\Theta = 2\kappa/\sqrt{2}\int_{-\delta}^{-y_0}(y^2-y_0^2)^{-\frac{1}{2}}\,dy = \kappa\sqrt{2}\,\cosh^{-1}(\delta/\kappa)[\Delta D/D+(r_0/\rho)\sin\alpha]^{-\frac{1}{2}}.$$

(b.) $\underline{\Delta D/D + (r_0/\rho)\sin\alpha < 0}$.

The particles have sufficient momentum to pass through the outer concentric circle. Thus, we write

$$\Theta = \kappa/\sqrt{2}\int_{-\delta}^{\delta} (y^2 - y_0^2)^{-\frac{1}{2}} dy = \kappa\sqrt{2}\,\sinh^{-1}(\delta/\kappa)|\,\Delta D/D + (r_0/\rho)\,\sin\alpha|^{-\frac{1}{2}},$$

let

$$\mu = (\kappa/\delta)^2 \Delta D/D \quad \text{and} \quad \epsilon = (\kappa/\delta)^2 r_0/\rho ,$$

then we have

$$\phi = \frac{\Theta}{\kappa\sqrt{2}} = \cosh^{-1}[\mu + \epsilon\sin\alpha]^{-\frac{1}{2}}, \quad \mu + \epsilon\sin\alpha > 0 \qquad (13)$$

and

$$\phi = \Theta/\kappa\sqrt{2} = \sinh^{-1}|\mu + \epsilon\sin\alpha|^{-\frac{1}{2}}, \quad \mu + \epsilon\sin\alpha < 0. \qquad (14)$$

These then are approximate expressions for the detection probability as a function of α and the various geometric parameters.

B. Spectrometer Resolution

For the resolution in this experiment we must average Eqs. (13) and (14) over all values of α and of r_0 up to the radius of the proton beam. First consider a cylindrical source of radius r_0. For the approximations, Eqs. (13) and (14), the range $-\pi/2$ to $+\pi/2$ for α gives the same result as the other half of the range. Therefore we may express the intensity as

$$I = 1/\pi \int_{-\pi/2}^{+\pi/2} (\Theta/2\pi)\, d\alpha.$$

For better resolution we use a slit system with the detector. Let Θ' be the central angle subtended by this slit centered on the circle ρ. Then we have

$$I' \simeq 1/2\pi^2 \int_{-\pi/2}^{+\pi/2} (\Theta - \Theta')\, d\alpha.$$

This may be evaluated by numerical integration to obtain the resolution function for a cylindrical source. Mr. Michael Lourie has written a program for the IBM-650 computer to do this integration.

The calculated shapes for cylindrical sources of various radii have been verified experimentally by studies with a monoenergetic alpha source in a 40-in. spiral-orbit spectrometer.

One may calculate the resolution for a conical target by adding resolution curves for a series of cylinders of radii between zero and the beam radius, each weighted by its radius which is proportional to the surface area. For the present geometry, we find $\kappa = 0.98$, $\rho = 7.71$ in., d = 0.125 in., the proton beam radius = 0.0625 in., and $\Theta' \approx 0.47$ radians. Examples of the curves for three radii are shown in Fig. 20. The resolution function for the conical target is presented in Fig. 9, and should be accurate to within less than 5%. The zero position corresponds to particles originating at the axis with the proper momentum to follow a focal orbit. The right side of the curve represents the probability of detecting particles of higher momenta. The scale is in percent of the focal momentum or, equivalently, of the magnetic-field setting. Also in this energy range it is in percent of the energy setting.

The fact that two slit systems have been used in the focal circle does not alter the shape of the resolution curve within the accuracy of its calculation. Examination of the trajectories, Fig. 3, reveals that the added detector will interfere with the very long paths, but these have a small detection probability because of the magnetic dispersion. The curve in Fig. 21 is the detection probability as a function of angle for a collimated source of N^{12} positrons at an energy near the maximum counting rate. The most probable orbits cover a central angle of 160 deg before reaching the first slit. A path blocked by the added detector would have to turn through about 400 deg to reach the slit, and very few particles have the right initial conditions for such orbits.

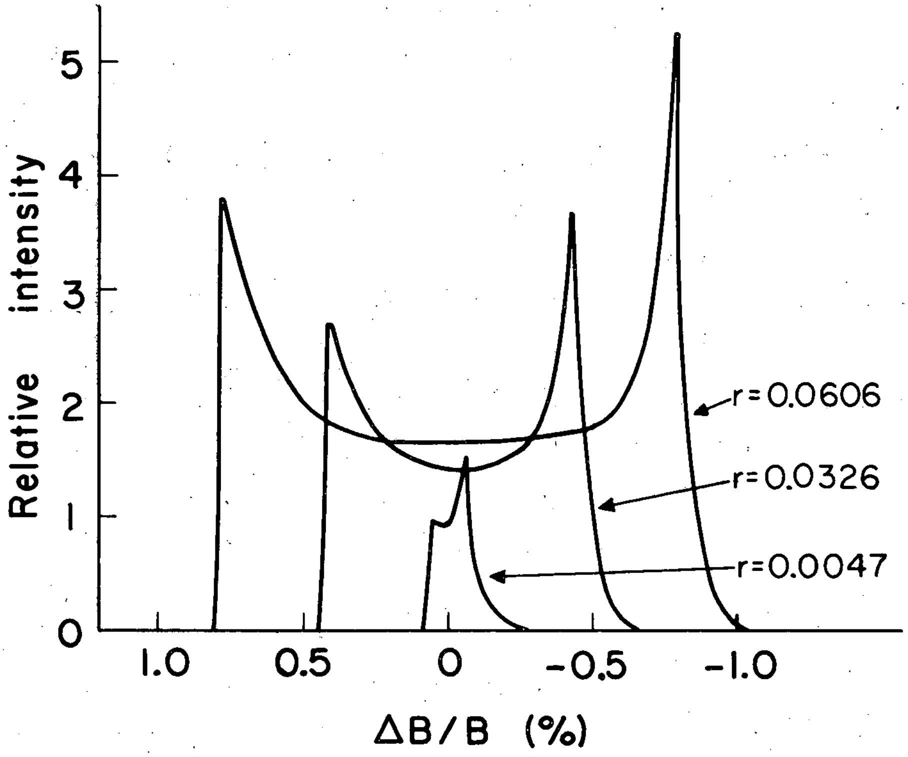

MU-15582

Fig. 20. Spectrometer resolution for cylindrical shells weighted by their radii. The "0" corresponds to the energy or momentum of a particle in the focal orbit. The probability of focusing higher-energy particles is represented by the right side of the curves.

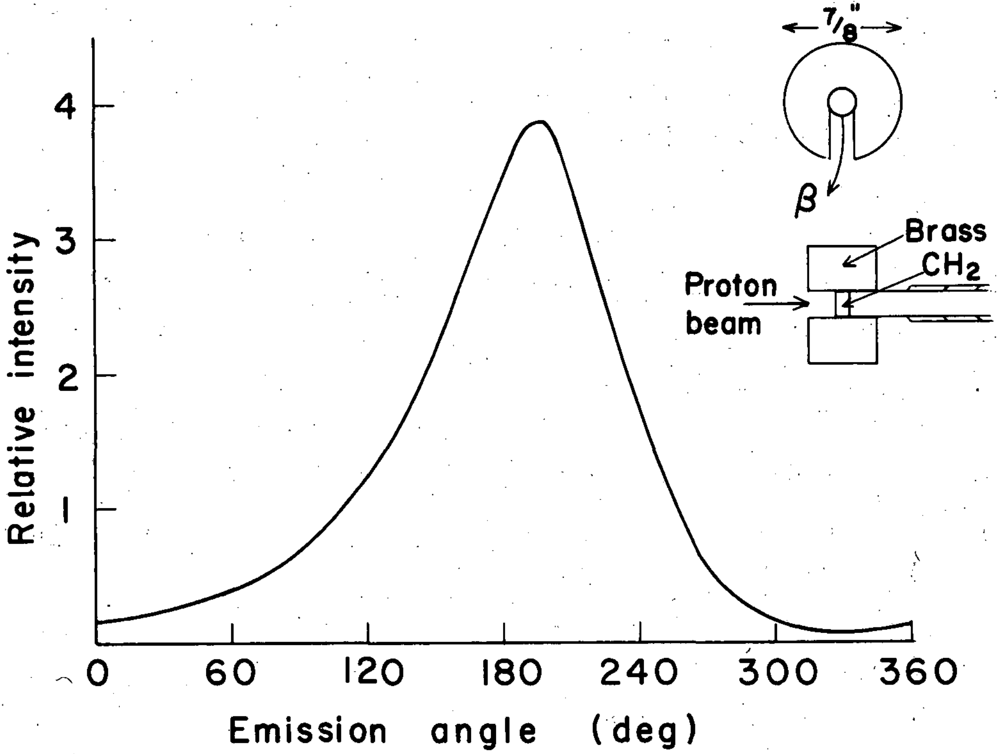

MU-15583

Fig. 21. Detection probability for Channel A as a function of emission angle. The target and collimator geometry are shown. The 0^o angle is defined by the first detector slit and the collimator direction, and the angles increase clockwise (Fig. 3).

X. REFERENCES

1. E. J. Konopinski and L. M. Langer in Annual Review of Nuclear Science (Annual Reviews, Stanford, 1953), Vol. 2, p. 261.
2. W. F. Hornyak and T. Lauritsen, Phys. Rev. 77, 160 (1950).
3. Luis W. Alvarez, Phys. Rev. 80, 519 (1950).
4. Francis C. Gilbert, Analysis of the Disintegration Products from the Reaction of 125-Mev Deuterons with Lithium Nuclei (Thesis), UCRL-2771, Oct. 1954; Phys. Rev. 93, 499 (1954).
5. N. W. Tanner, Phil.Mag. 1, 47 (1956).
6. Cook, Fowler, Lauritsen, and Lauritsen, Phys. Rev. 107, 508 (1957).
7. Luis W. Alvarez, Phys. Rev. 75, 1815 (1949).
8. Goro Miyamoto, Proc. Phys.-Math. Soc. Japan 24, 676 (1942).
9. Iwata, Miyamoto, and Kotani, J. Phys. Soc. Japan 2, 1 (1947) (in Japanese).
10. R. Sagane and W. Gardner, Spiral-Orbit Spectrometer, UCRL Translation-111, 1951.
11. B. Rossi and H. Staub, Ionization Chambers and Counters (McGraw-Hill, New York, 1949), p. 236.
12. Enrico Fermi, Z. Physik 88, 161 (1934).
13. National Bureau of Standards, Applied Math. Series 13, (1952).
14. Steven A. Moszkowski, Phys. Rev. 82, 35 (1951); Revs. Modern Phys. 25, 473 (1953).
15. Raymond T. Birge, Phys. Rev. 40, 207 (1932).
16. Herman Feshbach, Phys. Rev. 88, 295 (1952).
17. Rudolph M. Sternheimer, Phys. Rev. 88, 851 (1952).
18. Rudolph M. Sternheimer, Phys. Rev. 91, 256 (1953).
19. Rudolph M. Sternheimer, Phys. Rev. 103, 511 (1956).
20. L. Landau, J. Phys. (USSR) 8, 201 (1944).
21. E. J. Williams, Proc. Roy. Soc. (London) A 125, 420 (1929).
22. Goldwasser, Mills, and Hanson, Phys. Rev. 88, 1137 (1952).
23. Chen N. Yang, Phys. Rev. 84, 599 (1951).
24. William T. Scott, Phys. Rev. 76, 213 (1949).
25. H. Bethe and W. Heitler, Proc. Roy. Soc. (London) A 146, 83 (1934).

26. Lewis, Burchain, and Chang, Nature 139, 24 (1937).
27. Ogle, Brown, and Conklin, Phys. Rev. 71, 378 (1947).
28. Hughes, Hall, Eggler, and Goldfarb, Phys. Rev. 72, 646 (1947).
29. George C. Baldwin, Phys. Rev. 76, 182A (1949).
30. W. Rall and K. G. McNeill, Phys. Rev. 83, 1244 (1951).
31. Moak, Good, and Kunz, Phys. Rev. 85, 928 (1952).
32. Raymond K. Sheline, Phys. Rev. 87, 557 (1952).
33. D. St P. Bunbury, Phys. Rev. 90, 1121 (1953).
34. Pierre Bretonneau, Compt. rend. 236, 913 (1953).
35. R. M. Kline and D. J. Zaffarano, Phys. Rev. 96, 1620 (1954).
36. Dunning, Butler, and Bondelid, Bull. Am. Phys. Soc. 1, 328 (1956); Phys. Rev. 110, 1076 (1958).
37. *American Institute of Physics Handbook*, D. E. Grey, Ed., (McGraw-Hill, New York, 1957), Sect. 8, p. 56.
38. John A. Wheeler, Phys. Rev. 59, 27 (1941).
39. Bonner, Evans, Malich, and Risser, Phys. Rev. 73, 885 (1948).
40. Nilson, Jentschke, Briggs, Kerman, and Snyder, Phys. Rev. 109, 850 (1958).
41. D. S. Bayley and H. R. Crane, Phys. Rev. 52, 604 (1937).
42. R. T. Frost and S. S. Hanna, Phys. Rev. 99, 8 (1955).
43. A. H. Armstrong and G. M. Frye, Jr., Phys. Rev. 103, 335 (1956).
44. Lothar W. Nordheim, Phys. Rev. 78, 294 (1950).
45. John A. Wheeler, Phys. Rev. 52, 1083 (1937).
46. Dieter Kurath, Phys. Rev. 101, 216 (1955).
47. C. M. Class and S. S. Hanna, Phys. Rev. 89, 877 (1953).
48. M. Morita and M. Yamada, Progr. Theoret. Phys. (Kyoto) 13, 114 (1955).
49. Hanna, LaVier, and Class, Phys. Rev. 95, 110 (1954).
50. R. A. Becker and E. R. Gaerttner, Phys. Rev. 56, 854A (1939).
51. J. V. Jelley and E. B. Paul, Proc. Cambridge Phil. Soc. 44, 133 (1948).
52. Brolley, Cooper, Hall, Livingston, and Schlacks, Phys. Rev. 83, 990 (1951).

53. Cook, Penfold, and Telegdi, Phys. Rev. 104, 554 (1956).

54. E. Norbeck, Jr., Bull. Am. Phys. Soc. 1, 329 (1956).

55. Ajzenberg-Selove, Bullock, and Almqvist, Phys. Rev. 108, 1284 (1957).

56. Dols, Skiff, and Watson, A Temperature-Regulated Bismuth Resistor for Magnetic-Field Measurements, UCRL-3729, June 1957.

57. H. Margenau and G. M. Murphy, The Mathematics of Physics and Chemistry (Van Nostrand, New York, 1943), p. 460.